Title

A Tale of Two Rapidly Intensifying Supertyphoons: Hagibis (2019) and Haiyan (2013)

Journal

Bulletin of the American Meteorological Society, 102(9)

ISSN

0003-0007

Authors

Lin, I-I

Rogers, Robert F

Huang, Hsiao-Ching

et al.

Publication Date

2021-09-01

DOI

10.1175/bams-d-20-0223.1

BAMS Article

A Tale of Two Rapidly Intensifying Supertyphoons

Hagibis (2019) and Haiyan (2013)

I.-I. Lin, Robert F. Rogers, Hsiao-Ching Huang, Yi-Chun Liao, Derrick Herndon, Jin-Yi Yu, Ya-Ting Chang, Jun A. Zhang, Christina M. Patricola, Iam-Fei Pun, and Chun-Chi Lien

ABSTRACT: Devastating Japan in October 2019, Supertyphoon (STY) Hagibis was an important typhoon in the history of the Pacific. A striking feature of Hagibis was its explosive rapid intensification (RI). In 24 h, Hagibis intensified by 100 knots (kt; 1 kt ≈ 0.51 m s^{-1}), making it one of the fastest-intensifying typhoons ever observed. After RI, Hagibis's intensification stalled. Using the current typhoon intensity record holder, i.e., STY Haiyan (2013), as a benchmark, this work explores the intensity evolution differences of these two high-impact STYs. We found that the extremely high prestorm sea surface temperature reaching 30.5°C, deep/warm prestorm ocean heat content reaching 160 kJ cm^{-2}, fast forward storm motion of ~8 m s^{-1}, small during-storm ocean cooling effect of ~0.5°C, significant thunderstorm activity at its center, and rapid eyewall contraction were all important contributors to Hagibis's impressive intensification. There was 36% more air–sea flux for Hagibis's RI than for Haiyan's. After its spectacular RI, Hagibis's intensification stopped, despite favorable environments. Haiyan, by contrast, continued to intensify, reaching its record-breaking intensity of 170 kt. A key finding here is the multiple pathways that storm size affected the intensity evolution for both typhoons. After RI, Hagibis experienced a major size expansion, becoming the largest typhoon on record in the Pacific. This size enlargement, combined with a reduction in storm translational speed, induced stronger ocean cooling that reduced ocean flux and hindered intensification. The large storm size also contributed to slower eyewall replacement cycles (ERCs), which prolonged the negative impact of the ERC on intensification.

KEYWORDS: Air-sea interaction; Atmosphere-ocean interaction; Hurricanes/typhoons; Sea surface temperature; Tropical cyclones

https://doi.org/10.1175/BAMS-D-20-0223.1

Corresponding author: Dr. I-I Lin, iilin@as.ntu.edu.tw; Dr. Robert Rogers, robert.rogers@noaa.gov

Supplemental material: https://doi.org/10.1175/BAMS-D-20-0223.2

In final form 9 April 2021

AFFILIATIONS: Lin, Huang, Liao, Chang, and Lien—Department of Atmospheric Sciences, National Taiwan University, Taipei, Taiwan; **Rogers**—NOAA/AOML/Hurricane Research Division, Miami, Florida; **Herndon**—Cooperative Institute for Meteorological Satellite Studies, University of Wisconsin–Madison, Madison, Wisconsin; **Yu**—Department Of Earth System Science, University of California, Irvine, Irvine, California; **Zhang**—NOAA/AOML/Hurricane Research Division, and Cooperative Institute for Marine and Atmospheric Studies, University of Miami, Miami, Florida; **Patricola**—Department of Geological and Atmospheric Sciences, Iowa State University, Ames, Iowa, and Climate and Ecosystem Sciences Division, Lawrence Berkeley National Laboratory, Berkeley, California; **Pun**—Institute of Hydrological and Ocean Sciences, National Central University, Taoyuan, Taiwan

In October 2019, Supertyphoon (STY)[1] Hagibis badly damaged Japan (including Tokyo) and became the second costliest typhoon on record in the Pacific.[2] Hagibis was also the second deadliest typhoon to affect Japan (next to Tip in 1979). This brings to mind another powerful STY, Haiyan, which devastated the Philippines with ~6,000 deaths in 2013 (Lander et al. 2014; Lin et al. 2014; Mori et al. 2014; Lagmay et al. 2015; Huang et al. 2017; Wada et al. 2018; Kuo et al. 2019; Tsujino and Kuo 2020). Though both are among the highest-impact category-5 STYs in the history of the Pacific and both experienced rapid intensification (RI) (Holliday and Thompson 1979; Kaplan and DeMaria 2003; Knaff et al. 2018), their intensity evolution was actually quite different, contributing to substantially different impacts at landfall.

Hagibis explosively intensified from 60 to 160 knots (kt; 1 kt ≈ 0.51 m s^{-1}) (tropical storm to category 5) between 1200 UTC 6 October and 1200 UTC 7 October 2019 (Fig. 1a). This 100-kt intensification in 24 h is 333% of the RI threshold [30 kt (24 h)$^{-1}$; Kaplan and DeMaria 2003] and is close to the record-breaking intensification rate of 105 kt (24 h)$^{-1}$ for Hurricane Patricia of 2015 (Rogers et al. 2017).

After the impressive RI, Hagibis reached its lifetime maximum intensity (LMI) of 160 kt (Fig. 1a). It soon passed over the Guam/Mariana Islands. On 8 October, its intensity weakened to 120 kt and then returned to ~135–145 kt until 0000 UTC 10 October. Subsequently, Hagibis's intensity started to decline as it moved northward over colder waters toward Japan (Ito et al. 2015). Upon landfall on 12 October, Hagibis's intensity was at category 2 (75 kt) (Fig. 1a). Though category 2 was still a significant wind speed, torrential rain was the main cause for damage (K. Tsuboki 2019, personal communication).

Haiyan also rapidly intensified, but not as fast as Hagibis, intensifying by 60 kt in 24 h (i.e., 70 to 130 kt between 0000 UTC 5 November and 0000 UTC 6 November 2013) (Fig. 1b).[3] In contrast to Hagibis, after RI, Haiyan continued to intensify, reaching a peak intensity of 170 kt (i.e., even to category-"6"[4] status) (Lin et al. 2014; Huang et al. 2017). This 170-kt LMI is still the intensity record holder for Pacific typhoons to date. Most unfortunately, Haiyan made landfall at this 170-kt wind and devastated the Philippines with deadly surge induced by this extreme wind interacting with local geography under preexisting high sea level condition (Lin et al. 2013a, 2014; Mori et al. 2014; Lagmay et al. 2015).

The apparent contrast in intensity evolution between these two STYs triggers our investigation. We will separate our discussion into two periods, the RI period (P1) and the post-RI period (P2). Specifically for P1, we ask why Hagibis was able

[1] STYs are typhoons of 1-min maximum sustained wind speed ≥130 kt, i.e., high category-4 and category-5 typhoons on the Saffir–Simpson scale. Because both cases are of category 5, they are STYs.

[2] Without factoring in inflation, Hagibis (2019) was the costliest typhoon (15 billion U.S. dollars) on record. However, if the inflation rate change is considered, Mireille (1991) was the costliest typhoon (10 billion in 1991 U.S. dollars and 18.8 billion in 2019 U.S. dollars). Data sources: https://en.wikipedia.org/wiki/Typhoon_Hagibis and https://en.wikipedia.org/wiki/Typhoon_Mireille.

[3] To compare with Hagibis, the RI period for Haiyan was also chosen to be within a 24-h window where Haiyan had the steepest intensification, and also of similar during-RI intensity category evolution as Hagibis.

[4] Currently, the highest category on the Saffir–Simpson scale is category 5 (i.e., ≥137 kt). Because Haiyan was much more intense than most "regular" category-5 TCs, it was proposed that Haiyan is more suitable to be classified as of "cateogy-6" status (Lin et al. 2014; Huang et al. 2017).

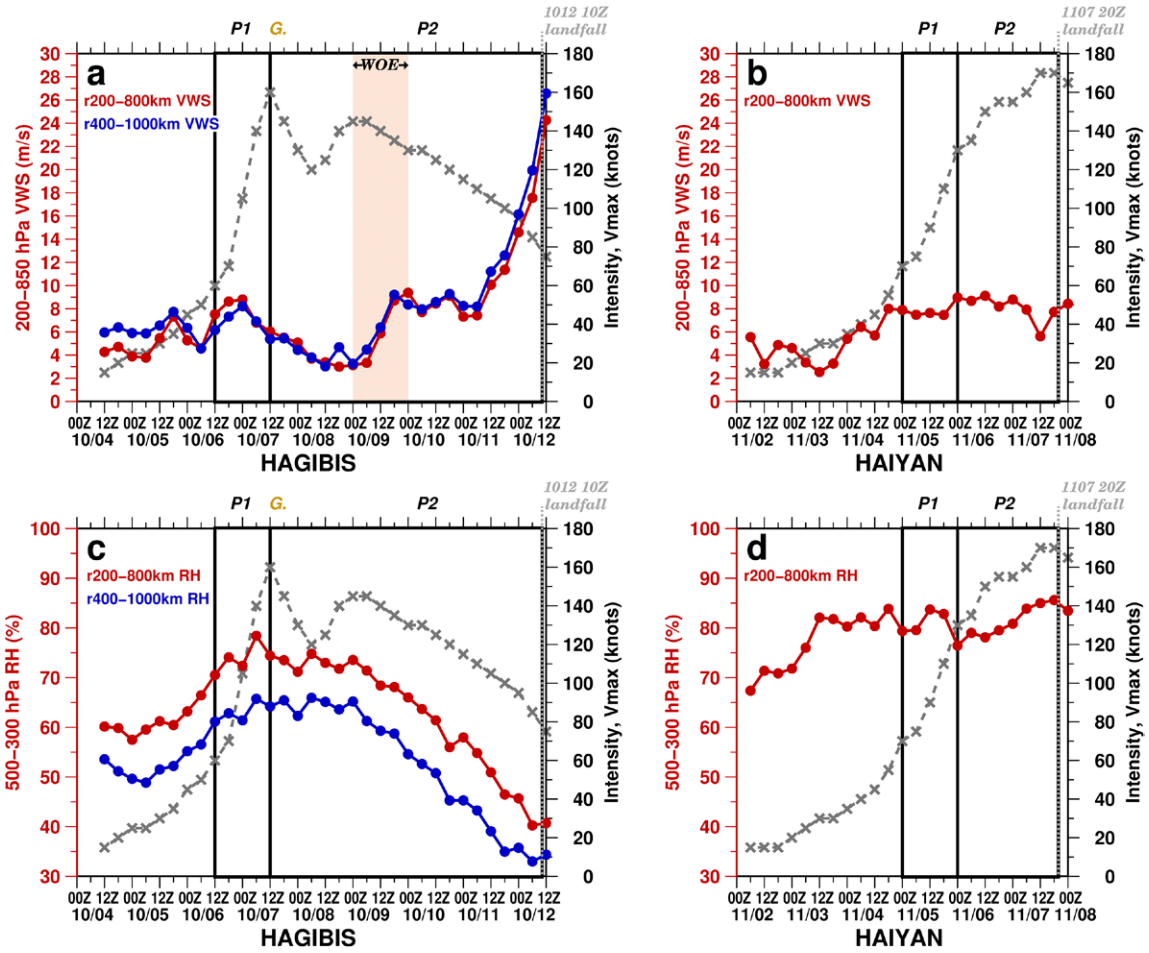

Fig. 1. (a) TC intensity time series (gray curve) of Hagibis (2019), with vertical wind shear (VWS) depicted. Due to Hagibis's large size, two types of VWS are calculated, i.e., averaged over a 200–800-km-radius ring (default approach), and averaged over a 400–1,000-km-radius ring (additional approach). "P1" denotes period 1 (RI period). "P2" denotes period 2 (post-RI period). "G" denotes passing over Guam/the Mariana islands. The pink bar depicts the time of the warm ocean eddy (WOE) passing. (b) As in (a), but for Haiyan (2013). (c),(d) As in (a) and (b), but for upper-level RH.

to intensify faster than Haiyan. For P2, we ask why, after a faster RI, Hagibis was not able to intensify further like Haiyan. This is especially curious because after RI, vertical wind shear (VWS) dropped to only 2–4 m s^{-1} for Hagibis (Fig. 1a). Hagibis also went over a prominent warm ocean eddy (WOE; Figs. 2c,d). This combination has been recognized to be highly favorable for intensification (Shay et al. 2000; Frank and Ritchie 2001; Lin et al. 2009a). Nevertheless, Hagibis did not intensify much.

Data and methods

Because tropical cyclone (TC) intensity is influenced by multiple factors spanning different spatiotemporal scales (Marks et al. 1998; Rogers et al. 2006; Dougherty et al. 2018), our investigation is based on four aspects: 1) large-scale atmospheric environment, e.g., VWS and relative humidity (RH) (De Maria et al. 2005; Knaff et al. 2005, 2018; Kaplan et al. 2010; Rogers et al. 2017); 2) large-scale pre-TC ocean environment and local-scale, during-TC air–sea interactions, e.g., pre-TC sea surface temperature (SST), pre-TC ocean heat content (OHC), TC's self-induced ocean cooling effect (during TC), and the during-TC air–sea fluxes (Shay et al. 2000; Cione and Uhlhorn 2003; Lin et al. 2005, 2013b; Wu et al. 2007; Goni et al. 2009; D'Asaro et al. 2014; Cione 2015; Jaimes et al. 2015; Tsuboki et al. 2015; Zheng et al. 2015; Zhang et al. 2017; Cheng and Wu 2020; Chih and Wu 2020); 3) vortex-scale

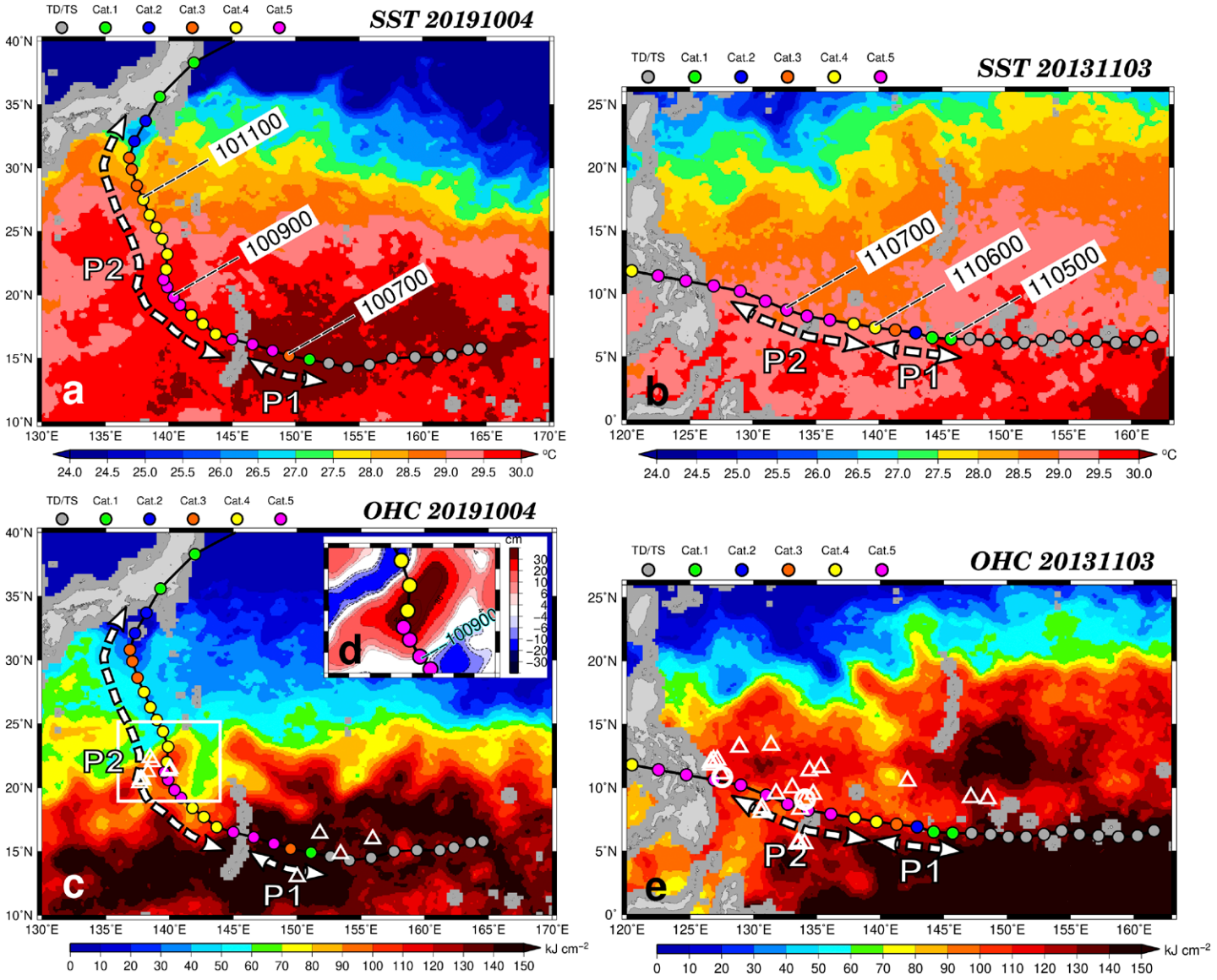

Fig. 2. (a),(b) Pre-TC SST (2 days before category 1) for Hagibis (Haiyan). (c),(e) As in (a) and (b), but for ocean heat content (OHC). Locations of in situ Argo floats are depicted as triangles (pre-TC Argo) and circles (during-TC Argo). (d) Satellite sea surface height anomaly (SSHA) map showing WOE. The location of (d) is shown as the white box in (c).

properties, e.g., storm size, translation speed (Uh), and eyewall replacement cycles (ERCs) (Chavas and Emanuel 2010; Chan and Chan 2012; Knaff et al. 2016; Chang and Wu 2017; Molinari et al. 2019; Shen et al. 2021); and 4) convective-scale features, e.g., radial location of deep convection (Rogers 2010; Rogers et al. 2013, 2015, 2016; Miyamoto and Takemi 2015; Kanada et al. 2017; Hu and Wu 2020; Peng and Wu 2020).

For observations, atmospheric environmental data are from the U.S. National Centers for Environmental Prediction Climate Forecast System Reanalysis (NCEP CFSR; V2, 6-hourly and 1° data). VWS is calculated based on the 850- and 200-hPa wind difference, averaged over a ring area (200–800 km) from the TC center (De Maria et al. 2005; Rogers et al. 2017). Considering Hagibis's large size, VWS is also calculated over a 400–1,000-km ring for comparison. Similar to VWS, RH is calculated based on the same ring areas. RH is calculated at two levels, i.e., average at 500–700 hPa (midlevel) and average at 300–500 hPa (upper level) (Knaff et al. 2005; Rogers et al. 2017).

Ocean data are from the satellite microwave (MW) SST (cloud penetrating, daily and 25-km resolution; http://data.remss.com/SST/daily/mw/), satellite altimetry sea surface height anomaly

(SSHA; daily and 25-km resolution; https://marine.copernicus.eu/), and in situ Argo float temperature/salinity profiles (ftp://ftp.ifremer.fr/ifremer/argo/dac/). SSHA is used to identify preexisting warm and cold ocean eddies and for OHC derivation (Shay et al. 2000; Lin et al. 2008; Goni et al. 2009; Pun et al. 2007, 2014). Argo profiles are for both the pre-TC SST (searched within 8 days and 4° radius from the track), as well as the during-TC SST [searched within TC's transit time (see definition below) and within 200-km radius from track].

TC track, intensity, size, and Uh are from or derived from the U.S. Joint Typhoon Warning Center (JTWC)'s best track data (6 hourly). Size parameters include radius of maximum wind (RMW),[5] 50-kt-wind diameter (D50), and radius of 64-, 50-, and 34-kt winds (R64, R50, R34, respectively). Uh is calculated based on the two neighboring points. Advanced Scatterometer (ASCAT) data are also used for ocean surface wind field observation [courtesy of the NOAA NESDIS Satellite Application and Research (STAR) Ocean Surface Wind team].

Precipitation structure and distribution are assessed using passive microwave imagery at 85–91 GHz for ice scattering, which is a proxy for deep convection [courtesy of the U.S. Naval Research Laboratory (NRL)]. Convective activity is also observed using the infrared (IR) brightness temperature (Tbs) imagery from NRL. Other information on TC structure and the presence of ERCs is indicated by the Morphed Integrated Microwave Imagery (MIMIC) and the Automated Rotational Center Hurricane Eye Retrieval (ARCHER)/Microwave-based Probability of Eyewall Replacement Cycle (M-PERC) data (Kossin and DeMaria 2016; Wimmers and Velden 2016; Wimmers et al. 2018) of the U.S. Cooperative Institute for Meteorological Satellite Studies (CIMSS). The ERC signature was assessed based on a hybrid approach,[6] as it involves both subjective human interpretation (Hawkins and Helveston 2008; Kossin and Sitkowski 2009; Kuo et al. 2009; Sitkowski et al. 2011) on the completeness and thickness of an outer convective ring in the MIMIC microwave imagery animation and the objectively identified M-PERC ring score Hovmöller diagram showing contracting outer-ring features. Satellite infrared (IR) imagery are also used to provide additional details.

For numerical analyses, the 3D Price–Weller–Pinkel (PWP) ocean model (Price et al. 1986, 1994) is used to assess the TC's self-induced ocean coupling (cooling) effect (called cooling effect or cooling hereafter). It is a well-recognized model for this purpose. Its application over the WNP has also been validated during the Impact of Typhoon on Pacific (ITOP) field campaign (Lin et al. 2013b; D'Asaro et al. 2014). The cooling effect is governed by multiple factors including the pre-TC ocean temperature and salinity profiles, background ocean current, as well as TC attributes (i.e., wind speed, Uh, and size) (Price 1981; Lin et al. 2009b; Knaff et al. 2013; D'Asaro et al. 2014; Ko et al. 2014; Walker et al. 2014; Mei et al. 2015; Wu et al. 2016; Pun et al. 2018, 2019; Balaguru et al. 2020; Chang et al. 2020).

Here 3DPWP is run with wind forcing (including wind profile shape) from the JTWC, and according to TC transit time, i.e., D50 over Uh (Lin et al. 2008, 2013b), at each 6-hourly track location. Wind speed is the 10-min wind, converted from the original 1-min wind speed of the JTWC best track. The drag coefficient (Cd) used is the high wind Cd from Powell et al. (2003). Pre-TC

[5] TC-penetrating flights over the WNP are rare (Wu et al. 2005; D'Asaro et al. 2014; Ito et al. 2018). Kossin et al. (2007) examined the estimated errors for the RMW from best track data in the North Atlantic by comparing their values with that from aircraft reconnaissance. They found the mean absolute error of the estimated RMW is ~10 km.

[6] This hybrid approach was adopted because either subjective, human ERC identification or objective, machine-based (i.e., ARCHER/M-PERC) identification has its own respective advantages and disadvantages. ARCHER/M-PERC was developed because human identification is subjective and different interpreters may have different answers. Also, human identification is a qualitative binary classifier, i.e., only "yes" or "no" for ERC occurrence is provided. However, the ARCHER/M-PERC approach is based on a quantitative model, which offers quantitative measure of ERC occurrence probability. It is a full model which also takes into account TC's intensity as well as previous image evolution. In addition, ARCHER/M-PERC can effectively and concisely organize the large amount of information in the microwave image sequence/animation into one Hovmöller diagram for convenient viewing. Thus, this automatic machine-based tool also reduces the tedious/time-consuming human interpretation tasks in ERC identification. Nevertheless, like all models, this automatic model is not perfect and due to the complex nature of ERC features (e.g., rainbands), the confusion/variability from various noise sources (e.g., diurnal pulses), and satellite sensor resolution issue on TC eye-resolving, human interpretation is still important. Therefore, we adopt this complementary, hybrid approach.

temperature and salinity profiles are from the pre-TC Argo observations. Two observed runs (experiments 1 and 2), i.e., one for each STY, are conducted using inputs based on the respective JTWC observations and the pre-TC Argo. These results are discussed in the main text. Additional sensitivity tests (i.e., experiments 3–6) are conducted in the online supplement (https://doi.org/10.1175/BAMS-D-20-0223.2) to provide further details. A summary of the experimental design is in appendix A.

After running the 3DPWP, the during-TC SST, i.e., pre-TC SST minus cooling, is obtained. This during-TC SST (can be called in-storm SST) are then used with the NCEP near-surface air temperature and humidity data for air–sea sensible and latent heat flux (SHF and LHF) estimation (Black et al. 2007; Lin et al. 2013b; D'Asaro et al. 2014; Cione 2015; Jaimes et al. 2015; Zhang et al. 2017). SHF and LHF are calculated based on the bulk aerodynamic formulas under high wind conditions. The exchange coefficients used are from Zhang et al. (2008). Near-surface (10-m) air temperature and humidity[7] are obtained from converting the NCEP sigma 995 level (~40-m) data to 10 m (Fig. ES1 in the online supplement), using the observed relationship from a large amount of historical TC inner-core dropsonde observations (Zhang et al. 2013, 2020) in category-4 and category-5 TCs in the North Atlantic, and averaged in the RMW region.

Additional information on data and methods is found in appendixes A–E.

[7] NCEP data are used in the absence of aircraft measurements. We acknowledge the possible uncertainty involved in the reanalysis data but do what we can to enhance the accuracy, e.g., converting the NCEP sigma-995-level data to 10 m.

Results

RI period (P1). We first examine VWS. As in Fig. 1a, Hagibis's VWS fluctuated between 6 and 9 m s^{-1} during RI. Haiyan had less fluctuation, remaining between 7 and 8 m s^{-1} (Fig. 1b). The averaged VWS was 7.6 (7.9) m s^{-1} for Hagibis (Haiyan). It appears that both cases were able to undergo RI under moderate VWS and the difference in VWS was small. As for the RH condition, Hagibis's RH was even lower than Haiyan's (Figs. 1c,d and ES2 in the online supplement); thus RH also cannot explain the faster RI in Hagibis than Haiyan.

Checking the pre-TC ocean conditions, very warm pre-TC SST of ~30°–30.5°C for Hagibis (Fig. 2a) and high potential intensity (PI; Bister and Emanuel 1998) of ~88 m s^{-1} were found. The pre-TC SST (PI) for Haiyan was also favorable, i.e., ~29°–29.5°C in Fig. 2b (~80 m s^{-1}), though not as high as for Hagibis. Hagibis's pre-TC OHC was also higher, i.e., ~140–160 kJ cm^{-2} (Fig. 2c) versus ~115–135 kJ cm^{-2} for Haiyan (Fig. 2e). Therefore, pre-TC ocean conditions were excellent for both STYs, though Hagibis's were even better. In fact, the pre-TC ocean conditions for Hagibis were among the most favorable ever observed in category-5 typhoons over the WNP (Lin et al. 2008, 2014; Pun et al. 2013; D'Asaro et al. 2014). Also, both storms had pre-TC OHCs comparable to those found for Hurricane Patricia (Rogers et al. 2017). As in Shay and Brewster (2010), eastern North Pacific (where Patricia was) is characterized by high upper-ocean stratification and a revised OHC parameter with inclusion of the stratification factor, called "equivalent" OHC, was proposed. Therefore, besides regular OHC, E-OHC was also calculated and pre-TC E-OHC of the three TCs was similar and comparable (see section "Equivalent OHC estimation" in the online supplement).

Vertical temperature profiles from the pre-TC in situ Argo floats (Fig. 3a) confirm the better pre-TC ocean thermal condition for Hagibis. However, this does not necessary guarantee there will be more energy (through air–sea fluxes) for Hagibis's RI, because the key period is "during intensification" and the contribution from cooling needs to be included (Price 1981; Lin et al. 2013b; D'Asaro et al. 2014; Huang et al. 2015). As such the actual parameter needed is the during-TC SST (pre-TC SST minus cooling) and not just the pre-TC SST. Three sources of

during-TC SST, i.e., 3DPWP output, in situ Argo observation (if found), and MW SST, were examined and used in the flux calculation.

Figures 3c and 3d illustrate the 3DPWP results for both typhoons. In general, due to the fast Uh (7.7–7.8 m s^{-1}, Table ES1 and Figs. 4c,d) and preexisting deep/warm ocean, cooling was small in both cases. During-TC SST of ~29.8°C (blue dashed profile), corresponding to ~0.5°C cooling from the pre-TC SST of ~30.3°C (blue solid profile), was found for Hagibis (Fig. 3c, Table ES1). For Haiyan, during-TC SST was ~28.9°C (red dashed profile in Fig. 3d), i.e., ~0.1°C cooling from the pre-TC SST of ~29.0°C (red solid profile). Though in comparison Hagibis had stronger cooling (due to its larger size and pre-TC ocean profile shape), it had a warmer pre-TC SST (~30.3°C) to start with. Hagibis's during-TC SST was thus still about 0.9°C higher than Haiyan's. As in Table ES2, this difference in during-TC SST is a main contributor to the differences in air–sea humidity (Δq) and the latent heat flux between the two STYs. As a result, Hagibis has 36% more air–sea enthalpy (sensible + latent heat) flux (~1,250 vs 920 W m^{-2}) than Haiyan during RI (Fig. 5). A value of during-TC SST near 30°C under intense TC-ocean interaction is one of the highest reported over the WNP (Fig. 3c). During the ITOP field campaign, during-TC SST of ~29°C (i.e., lower) was observed in STY Megi (Pun et al. 2011; Lin et al. 2013b; D'Asaro et al. 2014). In short, because of Hagibis's high pre-TC SST and small ocean cooling (due to fast Uh over deep/warm ocean), Hagibis was able to have high during-TC SST and fluxes during its RI.

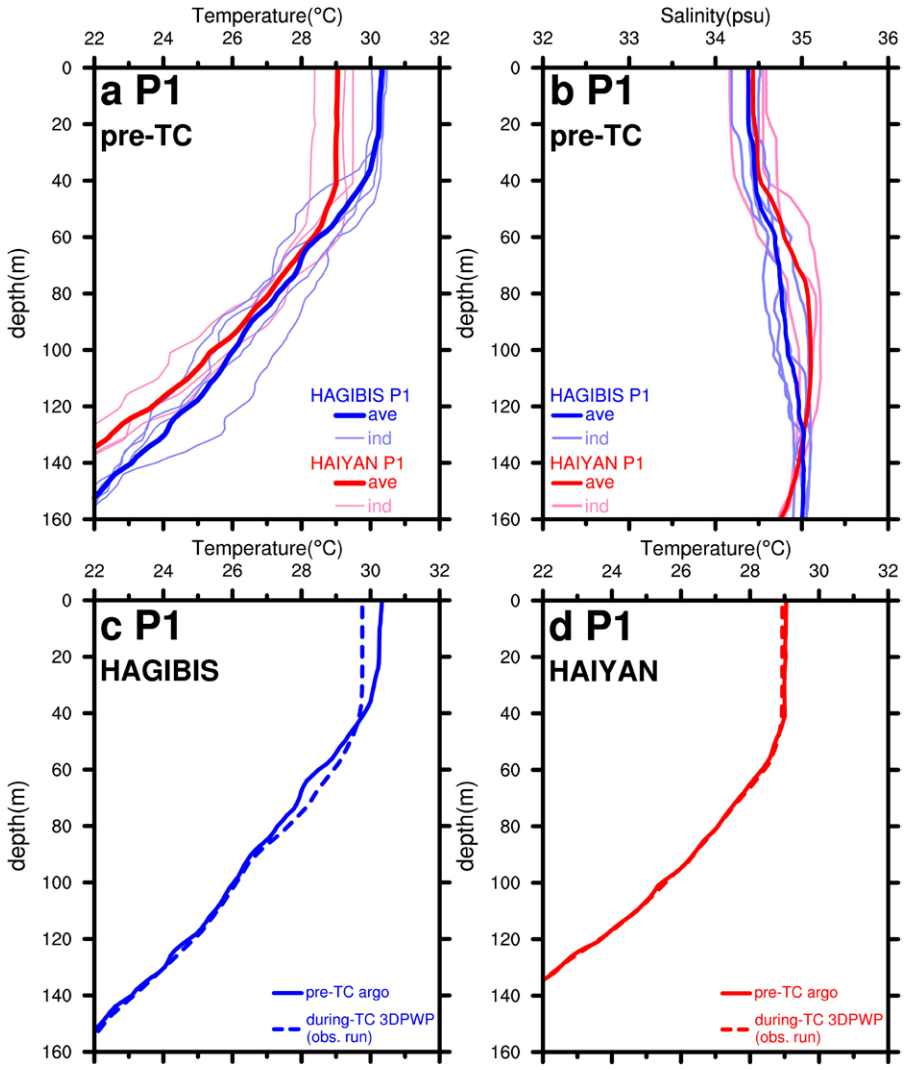

Fig. 3. Three-dimensional PWP simulations for period 1 (P1, i.e., RI period): (a) pre-TC ocean temperature profiles from in situ Argo floats (for locations, see Figs. 2c,e). Individual profiles (thin profiles) are averaged to obtain the two mean profiles (thick profiles). (b) As in (a), but for pre-TC salinity profiles. (c) Simulation result for Hagibis (i.e., experiment 1). The solid blue profile is the initial temperature profile [i.e., the mean blue profile in (a)]. The simulated, during-TC profile is the dashed blue profile. (d) As in (c), but for Haiyan (i.e., experiment 2). The initial pre-TC profile is in solid red and the simulated during-TC profile is in dashed red.

In terms of vortex structure, Hagibis had an RMW of ~45 km about 18 h prior to RI onset, while Haiyan's RMW was ~65 km (Figs. 4ab). In a study of intensification rates and wind structure for typhoons, Xu and Wang (2018) found that typhoons with smaller RMWs tend to have a higher intensification rate. By the time of RI onset (i.e., at the beginning of P1), both STYs had RMW values of ~30 km. Such small RMW values are consistent with theoretical

and observational studies showing small-RMW TCs are more likely to undergo RI (Emanuel 1989; Chen et al. 2011; Carrasco et al. 2014; Xu and Wang 2018). As RI began, both STYs had a substantial contraction of their RMW, but Hagibis's RMW contracted more rapidly than Haiyan (from ~30 to ~10 km in 6 h for Hagibis vs 18 h for Haiyan, respectively) during P1.

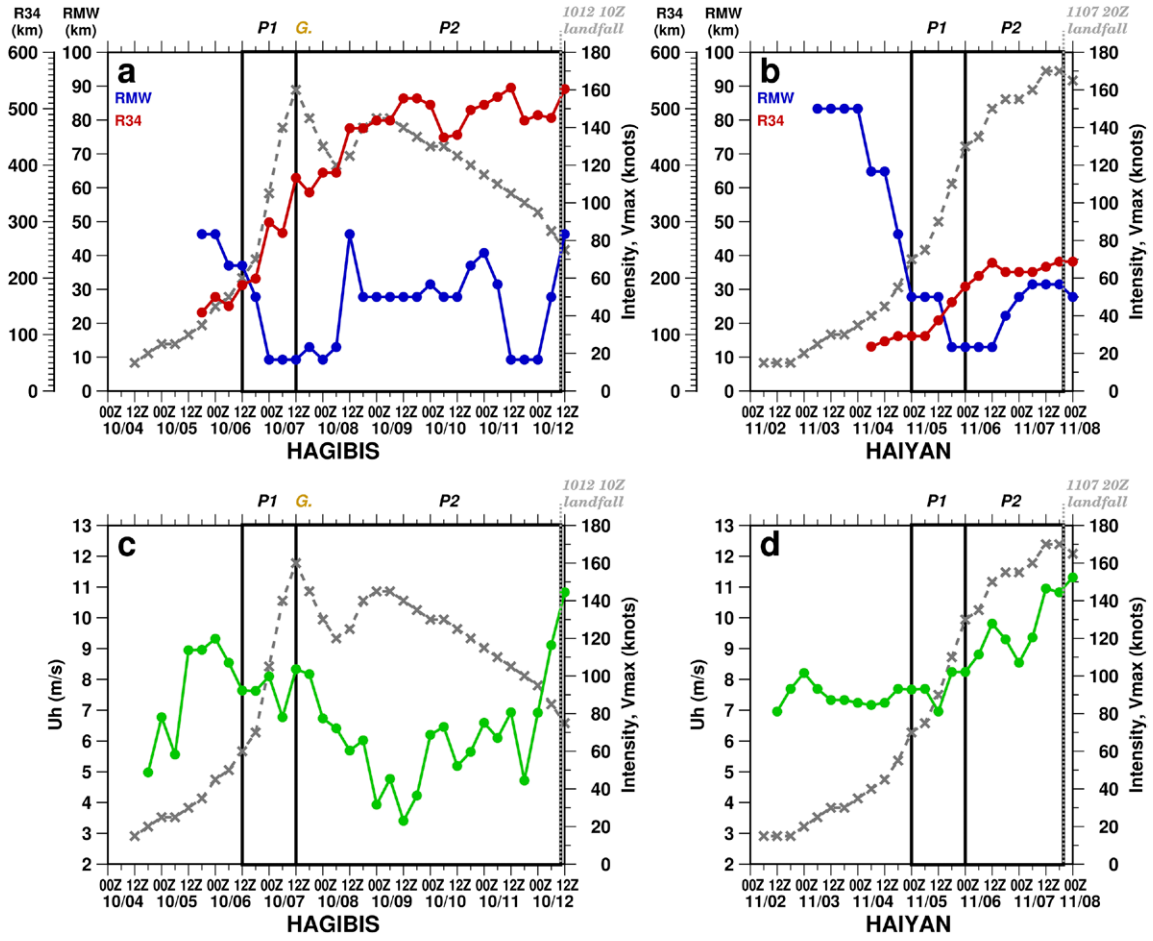

Fig. 4. (a),(b) As in Fig. 1, but TC intensity with two TC size parameters (RMW and R34). (c),(d) As in (a) and (b), but with Uh (translation speed). (left) Hagibis. (right) Haiyan.

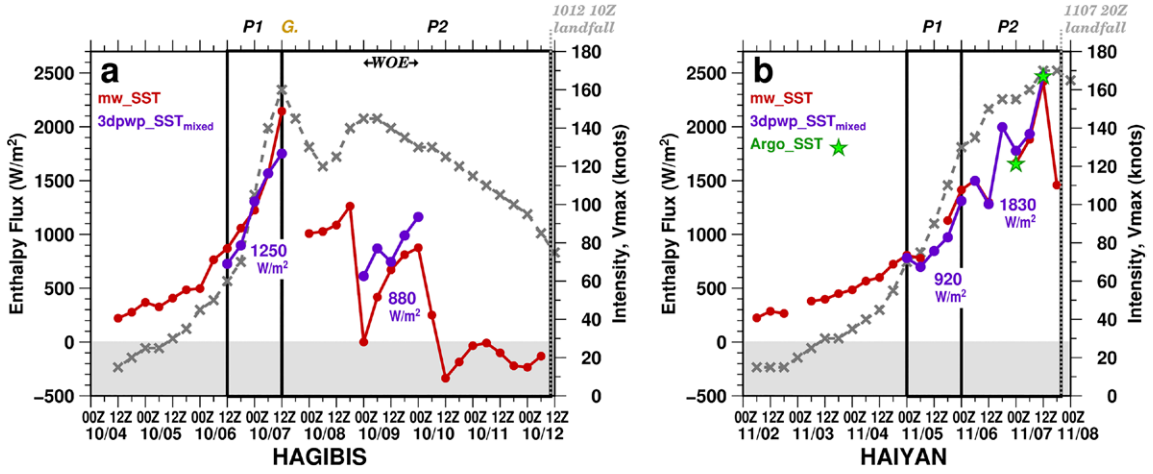

Fig. 5. As in Fig. 1, but for TC intensity (gray curve) with air–sea enthalpy (i.e., sensible + latent heat) fluxes. The fluxes are calculated based on three sources of during-TC SST, i.e., the 3DPWP result (in purple), Argo in situ SST (in green, where applicable), and satellite MW daily SST (in red). (a) Hagibis. (b) Haiyan.

The precipitation structure, as illustrated by 85–91-GHz microwave imagery, shows that Haiyan had a concentrated area of strong ice scattering, indicative of deep convection, surrounding a tiny eye with an estimated eye diameter of 40–50 km (Fig. 6b). This estimated eye diameter is roughly consistent with the estimated RMW from the best track dataset shown in Fig. 4b. Hagibis, by contrast, showed ice scattering maximized on the west side of, and closer to, the storm center (Fig. 6a). It is possible that this location of deep convection (also seen at later times during and just after P1; i.e., 0711, 1738, and 1944 UTC 7 October, cf. Figs. ES3, ES4), nearly coincident with Hagibis's center, led to the rapid contraction of the RMW shown in Fig. 4a. Deep convection located closer to the TC center has been linked to TC intensification due to peak diabatic heating being preferentially located within a region of high inertial stability (Pendergrass and Willoughby 2009; Vigh and Schubert 2009; Rogers et al. 2013) as well as being more likely to cause inward transport of angular momentum and rapid eyewall contraction (Smith and Montgomery 2016; Chen et al. 2018).

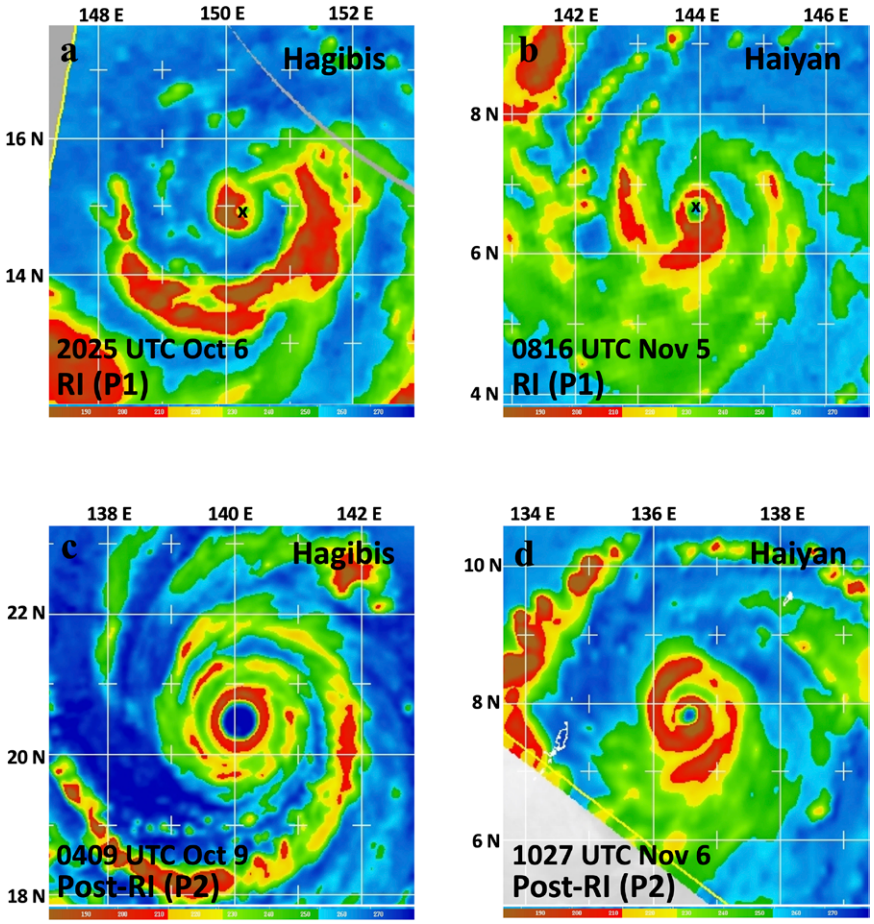

Fig. 6. (a) U.S. Department of Defense (DoD)'s Defense Meteorological Satellite Program (DMSP) F-17 satellite 91-GHz brightness temperature (shaded, K) for STY Hagibis, valid at 2025 UTC 6 Oct 2019. (b) As in (a), but for STY Haiyan, valid at 0816 UTC 5 Nov 2013. (c) As in (a), but for GCOM-W1 89 GHz, valid at 0409 UTC 9 Oct 2019. (d) As in (b), but for TRMM 85 GHz, valid at 1027 UTC 6 Nov 2013. Tick marks denote 1°; lines denote 2°. Black × in (a) and (b) denote the location of the center based on the best track. Each image is ~600 km on a side. All images are courtesy NRL site (www.nrlmry.navy.mil/tc-bin). P1 (P2) denotes period 1 (2).

The above suggests the small RMW, favorable radial location of deep convection, and rapid eyewall contraction contributed to Hagibis's intense RI. Besides the above, both STYs intriguingly had ERCs occur during the RI phase (Figs. 7, 8). As in Fig. 7, ERCs (i.e., ERC 1) for both STYs were identified, but they did not appear to limit the RI process, as has been shown in a recent Atlantic example, i.e., Irma (2017) (Fischer et al. 2020).

Post-RI period (P2). As described in the introduction, the question for P2 is why, after a faster RI, Hagibis was not able to intensify further like Haiyan. During 8–9 October, VWS even dropped to 2–4 m s^{-1}, and yet Hagibis's intensity fluctuated, suggesting other unfavorable factors existed that prevented Hagibis from further intensification (Fig. 1a). Early in P2 (8 October), Hagibis's intensity dropped to 120 kt as it encountered a weak cold ocean eddy (COE; in Fig. ES5 in the online supplement) while undergoing the second half of ERC1 (Fig. 7a). After Hagibis departed the COE and its ERC completed, Hagibis's intensity increased back to 140 kt at 1800 UTC 8 October. Hagibis subsequently encountered a prominent warm ocean eddy (WOE)

on 9 October (Figs. 1a, 2c,d). This WOE was characterized by very favorable SST of ~29.6°C and OHC ~103 kJ cm^{-2}, similar to Haiyan's favorable P2 pre-TC ocean condition of SST ~ 29.1°C and OHC ~ 109 kJ cm^{-2} (Figs. 2, 9a). Nevertheless, even with comparable pre-TC ocean thermal

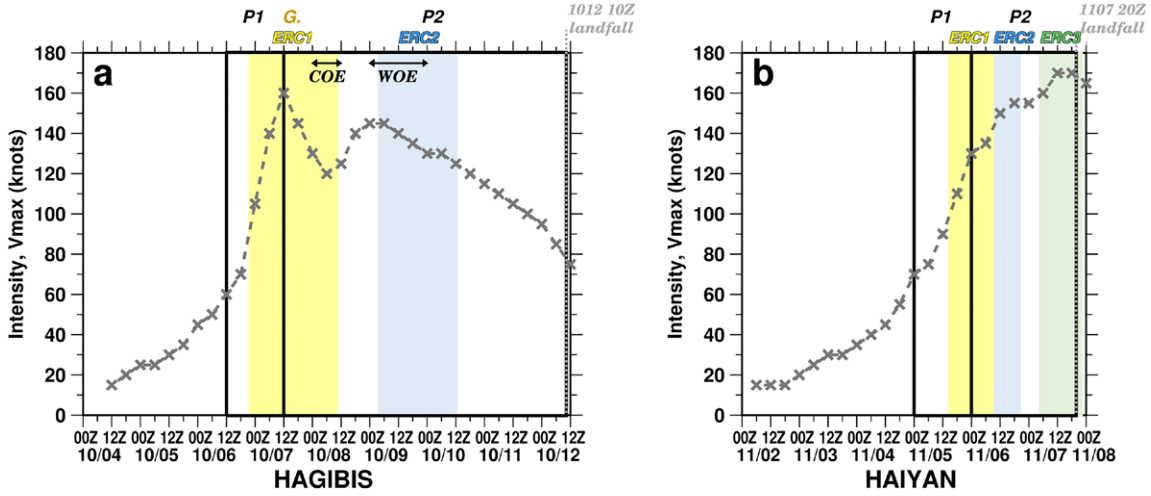

Fig. 7. As in Fig. 1, but for TC intensity and the ERC cycles. (a) Hagibis and (b) Haiyan. In (a), COE and WOE denote cold and warm ocean eddy passing time. ERC 1, 2, 3 is shown in yellow, blue, and green.

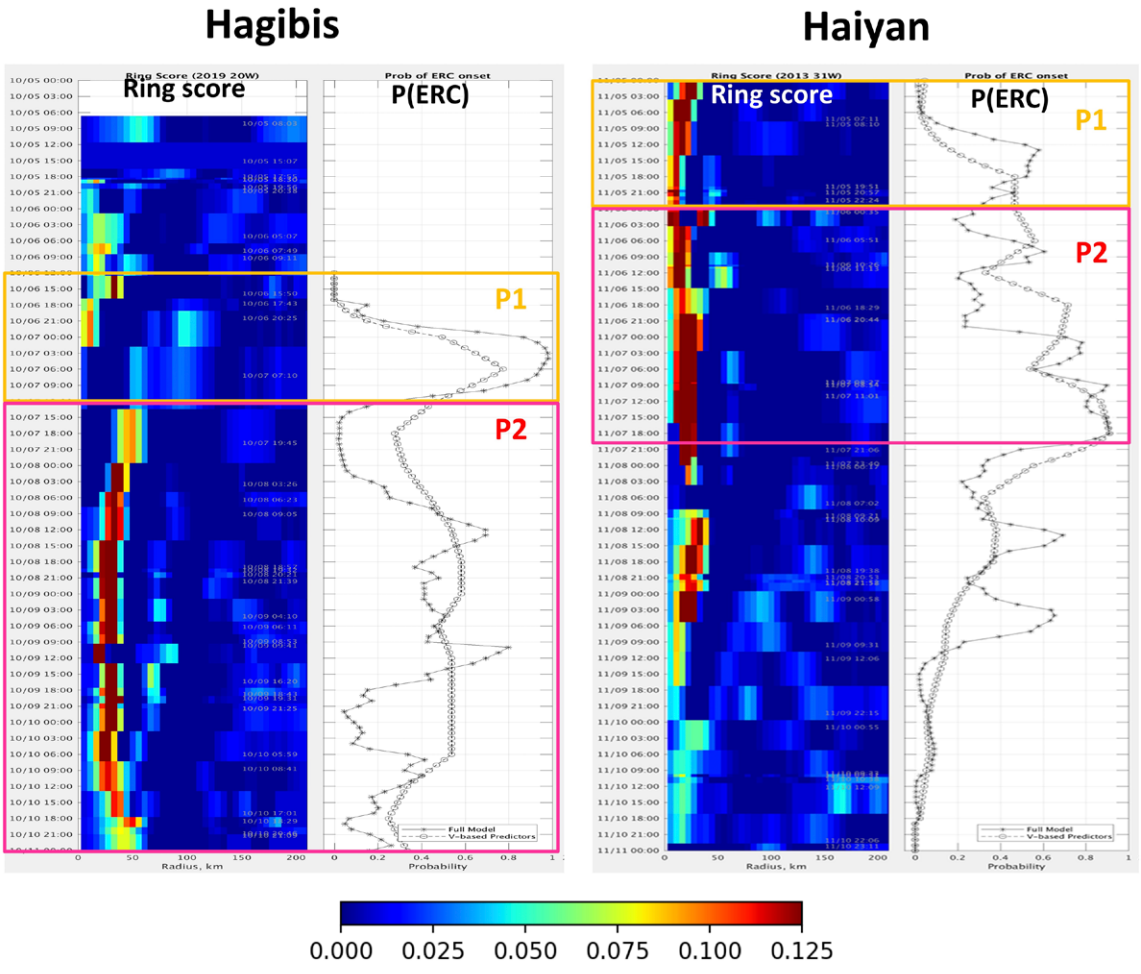

Fig. 8. Microwave Probability of Eyewall Replacement Cycle (M-PERC) ring scores and ERC probability for (left) Hagibis and (right) Haiyan. P1 (P2) denotes period 1 (2). Ring scores are derived from passive microwave 89-GHz imagery using ARCHER. Probabilities are produced using a logistic regression model based on ring score and TC intensity values.

conditions, Hagibis could not intensify much, while Haiyan intensified to 170 kt.

We then examined other possible distinguishing factors such as pre-TC ocean salinity, TC size, and TC translation speed. There was little difference in the pre-TC salinity conditions (Fig. 9b). However, considerable difference in TC size and Uh during P2 were found. As in Figs. 4a and 4b and Fig. ES6 in the online supplement, Hagibis became very large—2.5 times the size of Haiyan (i.e., R34 ~ 500 km vs ~200 km). Also, Hagibis's Uh dropped significantly to ~3–4 m s^{-1} while passing over the WOE on 9 October, compared with a 9.5 m s^{-1} for Haiyan (Figs. 4c,d). Both factors enhance the cooling effect, because the larger the size and the slower the Uh, the larger the cooling (Price 1981; Lin et al. 2009b; Walker et al. 2014; Pun et al. 2018; Chang et al. 2020). As in Fig. 9c, cooling of ~1.3°C was found (blue dashed profile), and the corresponding flux was 880 W m^{-2} over the WOE (9 October, Fig. 5a). If Hagibis was not so large and slow, but of similar size and Uh as Haiyan, cooling would only be ~0.3°C and the flux supply would be much higher, i.e., ~1,300 W m^{-2} (Fig. ES7c and Tables ES3 and ES4 in the online supplement).

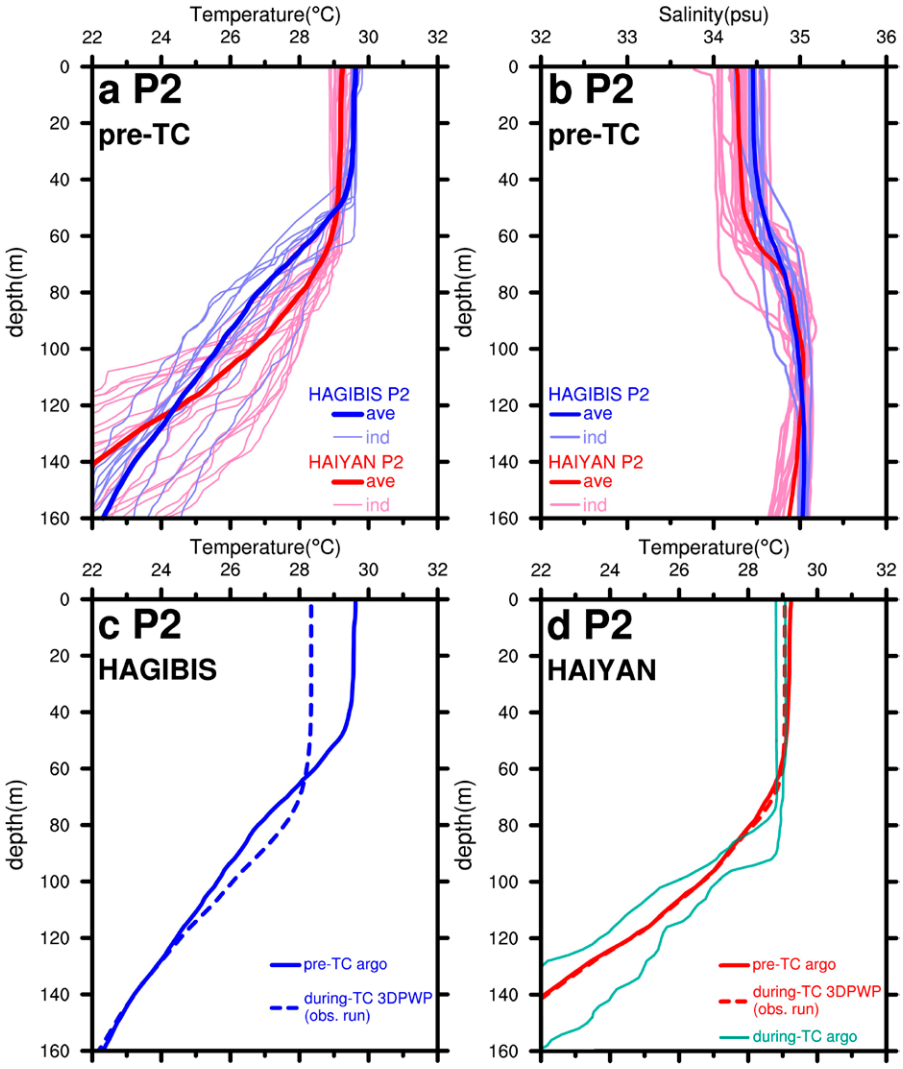

Fig. 9. As in Fig. 3, but for the 3DPWP simulations during period 2 (post-RI period). Two in situ during-TC Argo profiles are found for the Haiyan case [see green profiles in (d)].

As for Haiyan, the size increase during P2 was much less and its R34 remained around 200 km (Fig. 4b). Furthermore, Haiyan's Uh was even faster during P2 (i.e., ~9.5 m s^{-1}) than in P1 (Fig. 4d). Therefore, Haiyan's cooling remained small (0.2°C, dashed red profile in Fig. 9d), as confirmed by the in situ during-TC Argo observations (green profiles) and also reported in earlier work (Lin et al. 2014). There was thus ample flux (~1,830 W m^{-2})[8] to support further intensification to 170 kt (Fig. 5b). These flux results are also consistent with Zhang et al.'s (2017) finding in Hurricane Edouard (2014) over the Atlantic.

In brief, the significant size enlargement and Uh slowdown caused an enhanced ocean cooling effect to reduce air–sea fluxes to hinder Hagibis's intensification during P2. In contrast, Haiyan was able to remain compact in size and fast in Uh. Its cooling effect was therefore minimal and the associated fluxes were high.

In addition to the ocean-related factors described above, the atmospheric RH environment, vortex structure, and

[8] Because flux is also a function of wind speed (appendix C), Haiyan's higher wind speed also contributed to this high flux supply.

precipitation feature also supported the differing intensity evolutions of the two STYs during P2. Both mid- and upper-level RH (Figs. 1c,d and Fig. ES2) show that the environment around Hagibis dried substantially during P2, while RH values for Haiyan remained near 80%. Knaff et al. (2005) found that values of upper-level RH below ~60% were unfavorable for intensification, and our results are consistent with their finding (see blue curve in Fig. 1c, based on 400–1,000-km ring-area average, due to Hagibis's large size during P2).[9]

Figure 10 compares the NRL IR Brightness Temperature (Tb) imagery of the 2 STYs during P2. A distinct difference in convective activity is seen for both STYs, as Haiyan's cloud-top temperature was 10°C colder than Hagibis's. As for the microwave imagery, Figs. 6c and 6d show ice scattering during P2 for each storm. Haiyan shows significant ice scattering and deep convection around a small eye (~10-km RMW), with evidence of banding features wrapping around the northwest and into the southeastern quadrant (Fig. 6d). These banding features likely were associated with the secondary eyewall formation and subsequent second ERC events that Haiyan underwent (Figs. 7b, 8b). Though in existing literature (e.g., Wang 2009; Rozoff et al. 2012), a broader wind field is proposed to favor ERCs, the ERC occurrences in Haiyan suggest that ERCs can also occur in TCs of different sizes (e.g., compact TCs, Fig. 6d). In fact, three ERCs were identified in Haiyan; yet Haiyan's wind field remained compact during P2 (Fig. 4b) with little disruption to intensification (Figs. 7b).

[9] Though the discussion in P2 focuses on 9 October, it is also worth mentioning that toward the later part of P2 (i.e., 10–12 October), Hagibis's intensity continued to decline. This is consistent with the observed negative environment factors including increase in VWS, reduction in RH (Bukunt and Barnes 2015), and low OHC (Figs. 1a,c and 2a,c).

By contrast to Haiyan's very small RMW (~10 km) and compact wind field, Hagibis (Fig. 6c) showed a larger eye diameter of ~70–80 km and a clear indication of an outer eyewall, suggesting that Hagibis had also been experiencing ERCs (Figs. 7a, 8a). In addition, a pronounced outer band with extensive areas of deep convection spiraled out from the northwest quadrant

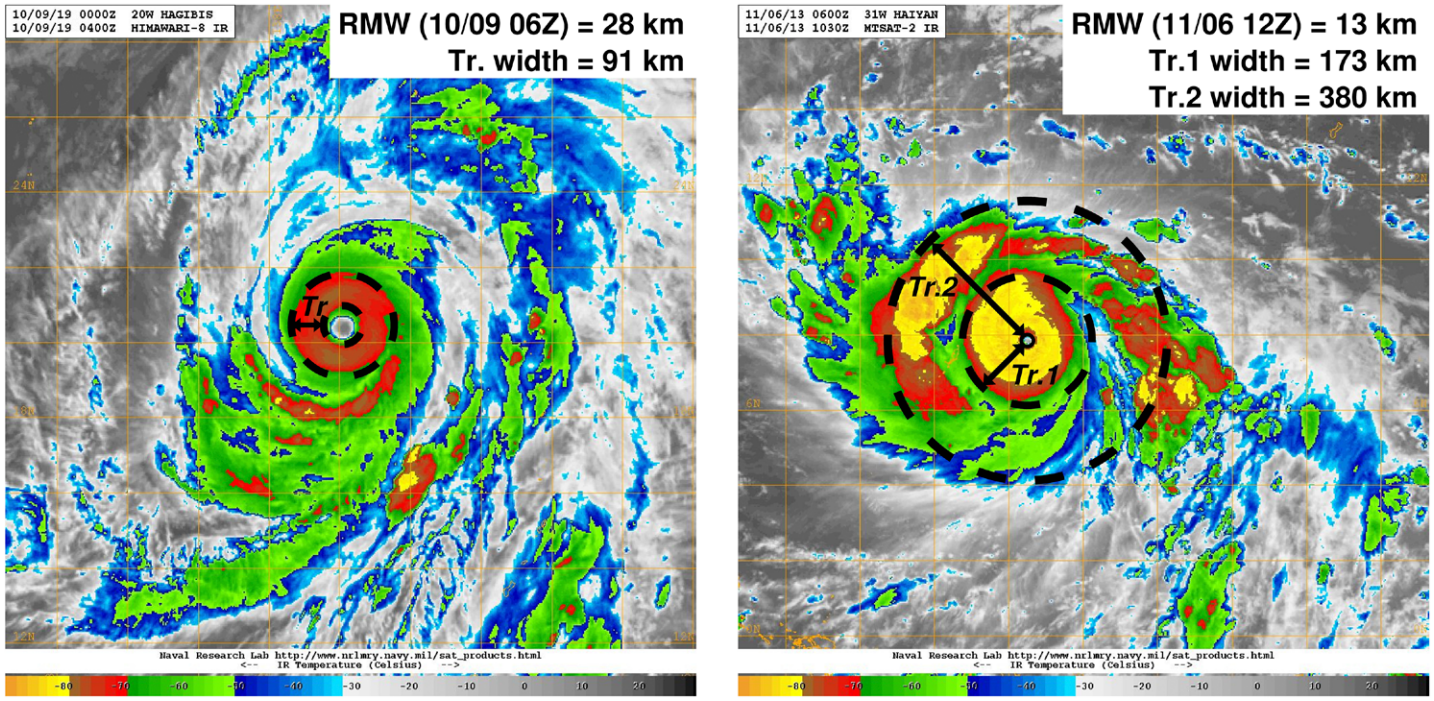

Fig. 10. Infrared brightness temperature images for (left) Hagibis and (right) Haiyan during P2 (courtesy: U.S. NRL; data sources: www.nrlmry.navy.mil/tcdat/tc19/WPAC/20W.HAGIBIS/ir/geo/1km/20191009.0400.hm8.x.ir1km.20WHAGIBIS.140kts-908mb-198N-1403E.100pc.jpg, www.nrlmry.navy.mil/tcdat/tc13/WPAC/31W.HAIYAN/ir/geo/1km/20131106.1030.mtsat2.x.ir1km.31WHAIYAN.135kts-922mb-76N-1380E.100pc.jpg).

all the way around to the southwest side of the storm between 100 and 200 km from the center. A secondary convective ring is clear in the imagery and a pronounced third banding feature wraps almost completely around the secondary ring.

This difference in the radial extent of precipitation between the two TCs was reflected in the wind radii shown in Figs. 4a and 4b: Haiyan showed a fairly compact wind field, with R34 only reaching ~250 km during its P2, while Hagibis had a much broader wind field, with R34 reaching nearly 550 km during its P2. It appears that though both STYs experienced ERCs during P2 (Figs. 7, 8),[10] the ERC processes in a smaller TC such as Haiyan evolved more quickly and the storm could overcome the inner-core disruption quicker and reorganize. Haiyan's structure was also able to remain compact. However, for a larger TC with a wider moat such as Hagibis, the process may take much longer and the negative impact from ERC to intensity (Sitkowski et al. 2011) appears more evident. A similar relationship between storm size, moat size, and intensity evolution during ERCs was found in an observational study of Hurricane Irma (2017) (Fischer et al. 2020). Irma underwent several ERCs, one of which occurred while Irma was continuing to undergo RI. During this ERC Irma had a small size (R34 ~ 150–200 km), similar to Haiyan, and a near-total lack of a moat region as measured by airborne Doppler radar. During an earlier ERC, which did slow Irma's intensification, there was a clear moat region.

[10] Detailed ERC imagery sequences are available for Hagibis (http://tropic.ssec.wisc.edu/real-time/mimtc/2019_20W/web/mainpage.html) and Haiyan (http://tropic.ssec.wisc.edu/real-time/mimictc/2013_31W/webManager/mainpage.html).

Composites of aircraft data in the Atlantic basin have also shown that a broader outer-core wind field favors steady-state TCs (Rogers et al. 2013; Martinez et al. 2017), likely through a reduction in radial inflow from enhanced inertial stability in the outer core that limits intensification. The large size and broad wind field in Hagibis compared to Haiyan is also shown in ASCAT observations (Fig. 11). For example, the radius of the R34 wind field for Hagibis's was ~520 km, while Haiyan's was ~210 km. Similar relationships of size differences were seen in the composite studies mentioned above. It should be noted, though, that this last point is speculative since there were no aircraft data for either storm to measure the strength of the radial flow.

The above results point to the importance of Hagibis's large size in limiting its intensification. We were thus curious to check "how big was Hagibis" among the WNP TCs. Since

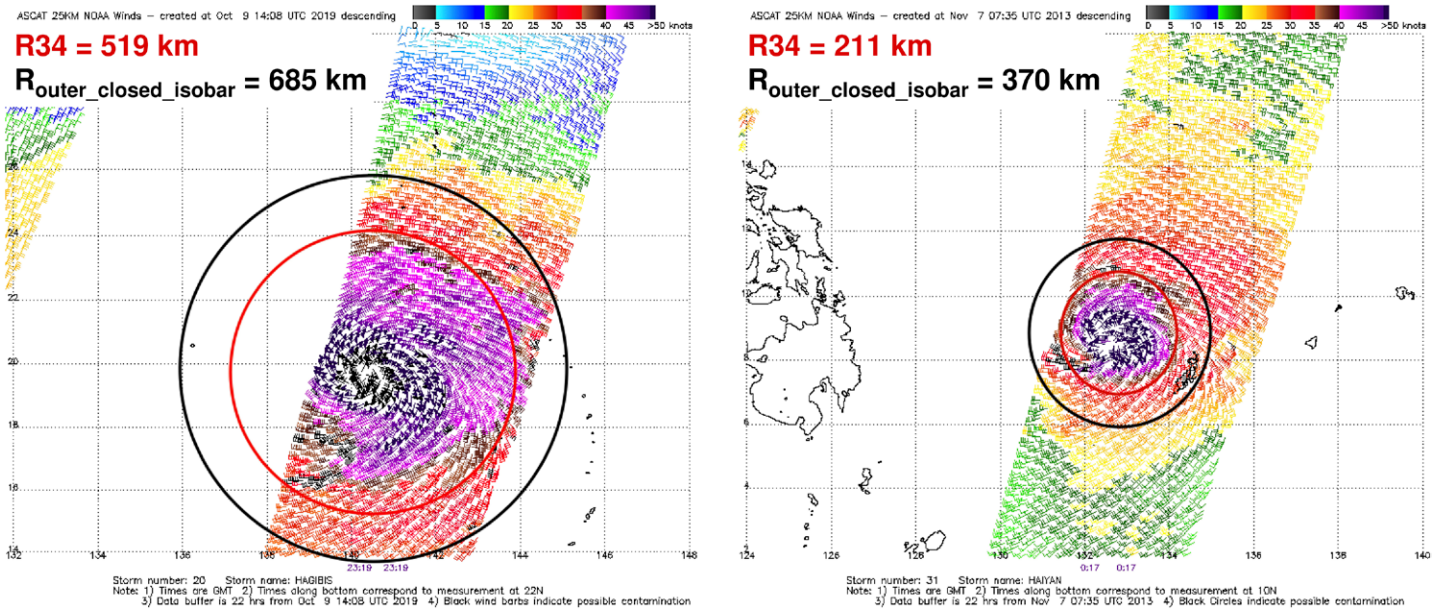

Fig. 11. Advanced Scatterometer (ASCAT) ocean surface wind vector images showing (left) Hagibis and (right) Haiyan during P2. (courtesy: NOAA NESDIS STAR ocean surface wind team).

the JTWC size records started from 2003,[11] we examined all 256 TCs (≥category 1) in the entire 17 years of (2003–19) record. For each case, we identify the "lifetime maximum R34" (LMR34). As in Fig. 12, we were also surprised to find that Hagibis is the largest TC (characterized by LMR34) in the entire period. It can also be seen that Haiyan belongs to the medium-sized category. We do not know why Hagibis was able to grow into such large size within such short time. This is certainly an important new question that warrants future exploration.

Conclusions

By investigating factors spanning multiple spatiotemporal scales (large-scale atmosphere, large- and local-scale ocean, vortex-scale TC size, translation speed, ERC, and precipitation-scale features), this research compares the intensity evolution of two important STYs, Hagibis (2019) and Haiyan (2013).

During the RI period (P1), Hagibis explosively intensified by 100 kt in 24 h, i.e., 333% of the RI threshold. Haiyan's RI (60 kt in 24 h) was also impressive, though slower than Hagibis. Two factors are identified to differentiate the RI between the two cases. First there was ~36% more air–sea flux for Hagibis than Haiyan, because Hagibis had higher during-TC SST of ~29.8°C (vs ~28.9°C for Haiyan) to contribute to this flux difference. This high during-TC SST for Hagibis was a result of a high pre-TC SST and a small ocean cooling effect (from fast translation speed of ~8 m s^{-1} over deep/warm ocean). The second factor is related to the vortex and precipitation structure. During P1, both STYs had an extremely small RMW (~10 km, a condition often favoring RI). However, Hagibis had a substantial area of deep convection nearly coincident with the center, a configuration known to be favorable for significant intensification. That placement of the deep convection, coupled with a rapid eyewall contraction, were likely critical contributors to Hagibis's explosive RI. By contrast, Haiyan had deep convection near the center, but it was in a ring surrounding the center at a radius consistent with the RMW. We also found during P1 that ERCs occurred in both STYs. Despite the presence of these ERCs, RI was not hindered in either case. These two new cases add support to the recent finding in Fischer et al.'s (2020) analysis of Hurricane Irma (2017), that ERCs indeed can occur, even during RI.

After the spectacular RI, Hagibis's intensity dropped and fluctuated during P2 (8–9 October). By contrast, Haiyan intensified all the way to the record-breaking 170 kt intensity (Lin et al. 2014). This is puzzling because Hagibis's pre-TC ocean conditions (e.g., SST and OHC) were comparable to Haiyan's.

[11] As JTWC size records started from 2003, during the earlier period (e.g., 2003 and 2004), the record may not be complete. Also, since size is a relatively new product, quality control is still ongoing (Sampson et al. 2017).

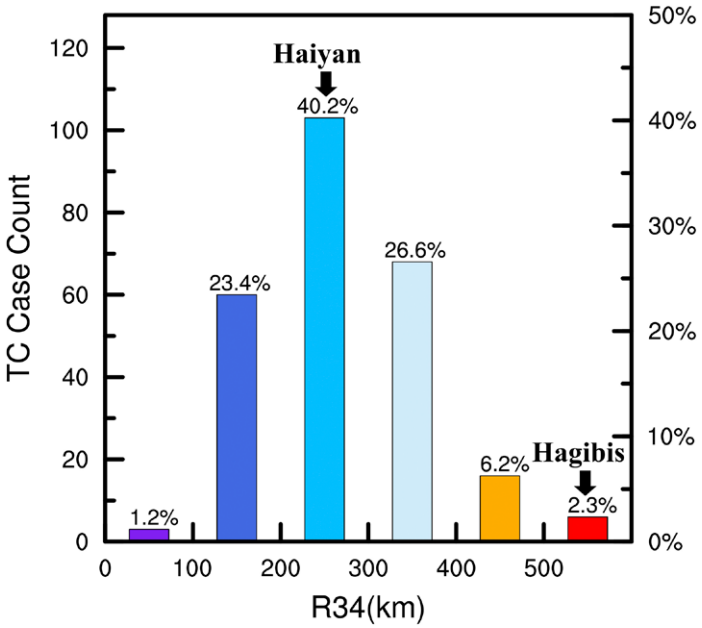

Fig. 12. Histogram showing the TC size distribution of the 256 TCs (category 1 and above) in the 17 years (2003–19) of the JTWC size records. The six bars represent 0–100, 100–200, …, 500–600 km. The size information is based on the "lifetime maximum R34" (LMR34), i.e., one LMR34 for each TC. LMR34 is identified when wind speed is ≥category 1. In the past 17 years, there were six TCs (2.3%) of LMR34 exceeding 500 km, with their ranking as follows: Hagibis (2019): 535 km (landfall point)/537 km (over ocean); Lan (2017): 505 km (excluding the transitional points from TC to extratropical storm); Choi-Wan (2015): 502 km (over ocean); Omais (2016): 500 km (over ocean); Mangkhut (2018): 500 km (over ocean but just before landfall); Chan-Hom (2015): 500 km (over ocean).

Hagibis's VWS even dropped to 2–4 m s^{-1} (much lower than Haiyan's). Hagibis also had a better start in P1. A surprise finding was how significant TC size was in differentiating between the intensity evolutions of each typhoon. After RI, Hagibis experienced a major size expansion (>200% enlargement, with R34 ~ 520 km), becoming the largest TC in the entire 17 years (2003–19) of JTWC's size records. In contrast, Haiyan's size remained compact (R34 ~ 200 km).

This large size expansion can hinder Hagibis's intensification in three different ways. First is the greater ocean cooling. Though Hagibis was over a prominent warm eddy, its large size together with a reduction in translation speed to 3–4 m s^{-1} enhanced the cooling effect to ~1.3°C. Without such a size enlargement and translation speed reduction, cooling would only be ~0.3°C and the flux supply would be much higher (1,300 vs 880 W m^{-2}).

Second is the slower ERC process. As compared to the smaller-size Haiyan, the ERC process of Hagibis was slower; thus, the negative impact from ERC appears to be more evident for Hagibis. For Haiyan, the ERC process was found to evolve more quickly and the storm appeared to overcome the inner-core disruption quicker and reorganize. Third is the possible reduction in radial inflow[12] from the broader tangential wind field and enhanced inertial stability in the outer core, as shown in Rogers et al. (2013).

Reflecting back on these results, we appreciate the complex interplay between environmental conditions, vortex-scale properties, and convective features. There is a delicate control on TC intensity via these multiscale interactions. Changes in vortex-scale properties (e.g., size) can impact TC intensification via interactions with the large-scale ocean environment through the ocean subsurface pathway, thus modifying the during-TC, local-scale air–sea interactions and flux to feedback to intensity change. Size change can also impact intensity via the ERC pathway, through differences in the ERC evolution time. Configuration of convective-scale feature, e.g., ice scattering at TC center, may also be associated with vortex-scale rapid eyewall contraction that favors RI. Certainly, these are only examples of nature's fascinating and coexisting cross-scale interaction pathways.

[12] Reduced inflow has been shown to be related to a broader tangential wind field and higher inertial stability, as observed by in situ aircraft observation over the North Atlantic (Rogers et al. 2013). Though there was no routine aircraft measurements over the western North Pacific to directly measure the radial flow for Hagibis and Haiyan, due to Hagibis's huge size, this possibility cannot be ignored and thus is mentioned here.

From the standpoint of predictive skill, a better understanding and prediction of these pathways contributes to improved skill on different time scales. A change in storm translation speed, passing over an ocean eddy, wind shear, environmental relative humidity, and other related factors are mostly external to the storm dynamics and serve to modulate intensity evolution over time scales ranging from 12 to 72 h or longer. The structure and location of deep convection, eyewall replacement cycles, storm size, eye size, etc., are the response of the storm to these external influences, and are part of the process of intensification. These are useful for prediction on the short (6–12 h) term. We believe further explorations of these pathways, and their multiscale interactions, will bring valuable benefits to TC intensity forecasting by providing a more holistic understanding of the TC intensity change, in particular rapid intensification.

Acknowledgments. We thank K. Tsuboki for helpful comments about Hagibis's rainfall impact. Thanks also to Jason Dunion for helpful discussions, to Tony Wimmers, Tim Olander, and Chris Velden for the M-PERC/ARCHER and related data. Thanks to the U.S. NCEP, JTWC, NRL, the Remote Sensing Systems, NOAA NESDIS, the European Union's Copernicus and the AVISO team, and the Argo team for providing essential datasets. I.L. acknowledges support from the Ministry of Science and Technology, Taiwan. R.R. acknowledges support from the U.S. NOAA Base Funds. C.M.P. acknowledges support from the U.S. Department of Energy, Office of Science, Office of Biological and Environmental Research, Climate and Environmental Sciences Division, Regional and Global Model Analysis Program, under Award

DE-AC02-05CH11231. We are also grateful to the three anonymous reviewers for their very insightful and constructive comments.

Appendix A: 3DPWP simulation

TC's size information is included in the 3DPWP via two parts: input wind profile and transit time (D50/Uh). JTWC's RMW, R64, R50, and R34 are used to characterize the wind profile. Cooling is obtained from area-averaging of the 2.5 × RMW region.

For both P1 and P2, six experiments were conducted. Experiments 1 and 2 are the essential runs, as in the main text. Experiments 3–6 are the additional sensitivity tests, as in the online supplement. These experiments are summarized below:

- Experiment 1—Hagibis's observed run: 3DPWP is run according to all the observed attributes of Hagibis, including TC attributes (e.g., wind, Uh, size) and pre-TC Argo temperature and salinity profiles.
- Experiment 2—Haiyan's observed run: As in experiment 1, but for Haiyan.
- Experiment 3—Size sensitivity run: Based on Hagibis's observed run, but replacing only Hagibis's size with Haiyan's size. This run thus represents the scenario that, if Hagibis's size was not so large as observed, but was of similar size as Haiyan, what would be the corresponding cooling effect.
- Experiment 4—Uh sensitivity run: As in experiment 3, but for the Uh replacement (i.e., instead of the size replacement).
- Experiment 5—Size + Uh sensitivity run: As in experiment 3, but replacing both size and Uh. This is to test the combined effect from size and Uh.
- Experiment 6—Salinity sensitivity run: As in experiment 3, but replacing Hagibis's prestorm salinity profile with Haiyan's prestorm salinity profile.

Appendix B: OHC

OHC is the integrated upper-ocean heat content from sea surface down to the depth of 26°C isotherm (D26) and is derived from satellite SST and SSHA data (Pun et al. 2007, 2013, 2014).

Appendix C: Air–sea flux calculation

The bulk formulas for SHF and LHF calculations are, SHF: $Q_s = C_H W (T_s - T_a) \rho_a C_{pa}$, LHF: $Q_L = C_E W (q_s - q_a) \rho_a L_{va}$, where C_H and C_E are the sensible and latent heat exchange coefficients under high wind condition (Zhang et al. 2008). As in Zhang et al. (2008), C_H (C_E) is 1.1 (1.2) × 10^{-3}. Other terms are as follows: W is ocean surface wind speed (1-min average, from JTWC), T_s and T_a are during-TC SST and near-surface air temperature, q_s and q_a are surface and air specific humidity, ρ_a, C_{pa}, and L_{va} are air density, heat capacity of the air, and latent heat of vaporization. The value of q_s is calculated from the during-TC SST.

Appendix D: VWS

Averaged vector wind over the ring area at each altitude (i.e., 850 and 200 hPa) is first calculated. The difference between the averaged wind vectors at the two altitudes is then obtained. VWS is calculated from the scalar of the wind vector difference.

Appendix E: ERC, M-PERC, and ARCHER ring score profiles

Ring structure is defined by the ice scattering signatures from the microwave 89-GHz data. This product, called M-PERC, is an experimental product that displays the ring score obtained from the CIMSS ARCHER algorithm (Wimmers and Velden 2016). Ring scores are derived from the 89-GHz imagery as part of the process of determining the TC center location in ARCHER. The scores are nondimensional values computed at each pixel annulus to determine ring

completeness. In addition to the ring's circular score, additions are made to the score based on the population and magnitude of Tbs within the ring. ARCHER ring scores are an objective measure of TC eyewall completeness and vigor and can thus be used to track the evolution the TC inner-core organization as well as potential secondary eyewall candidate rings. For M-PERC the ring scores out to 200 km are displayed as a Hovmöller diagram as a function of distance from the TC center. Values vary from 0 to 0.125. M-PERC uses these scores along with the time-evolving changes in the TC intensity to produce probabilities of the onset of an ERC (second column in Fig. 8). Two models are plotted to include the full model with all predictors and the second model that uses only TC intensity values. The display allows the analyst to objectively see the evolution of the TC inner and outer rings with intensification and contraction of the ring features leading to increased probability of an ERC event.

For example, the ERC periods noted in Fig. 7 are estimated based on the onset time of secondary eyewall formation (SEF) using the passive microwave imagery, to the time of completion of the process when the secondary eyewall has contracted and the inner eyewall no longer is indicated. This evolution is also seen in Fig. 8. Using the first ERC event (i.e., ERC 1) of Hagibis's as an example (Fig. 8, left), we explain below. Prior to the SEF/ERC onset, one can first see the development of the primary eye (i.e., the inner eye) in early 6 October. At 1500 UTC 6 October, the primary eye (in dark brown, i.e., strong ring score) started to contract inwardly from ~30 to <10 km, due to Hagibis's tiny eye at around 1800 UTC 6 October. Meanwhile, the secondary eye started (i.e., outer ring, in light green shade at a radius of ~125 km) to occur, at ~2100 UTC 6 October. Subsequently, the outer ring contracts inward and the inner-ring scores weaken and disappear around 1500 UTC 7 October in the ARCHER Hovmöller diagram (Fig. 8, left). Nevertheless, it should be noted that if from human identification in the satellite imagery sequence, ERC 1 completed at a later time, i.e., at ~1500 UTC 8 October, and not ~1500 UTC 7 October. This discrepancy is because ARCHER is unable to resolve the tiny inner eye feature of Hagibis beyond 1500 UTC 7 October, because sometimes the eye can be as small as one pixel in diameter in the microwave imagery. Human interpretation, however, can more sharply identify the relict inner eye feature, as well as factor in the TC eye information from other images (e.g., earlier/later microwave and satellite IR images when TC eye identification is possible). In other words, even in certain microwave images (due to coarse resolution), TC eye identification is not possible for both ARCHER and humans, because humans could make intelligent guesses from relict TC eye feature as well as including prior/later information from neighboring images, human beings still know the existence of the TC eye though they cannot directly see it. As mentioned in the main text, both objective (i.e., ARCHER) and subjective approaches have their own pros and cons and this example again highlights the importance of conducting the hybrid approach, to avoid using only one method.

References

Balaguru, K., G. R. Foltz, L. R. Leung, J. Kaplan, W. Xu, N. Reul, and B. Chapron, 2020: Pronounced impact of salinity on rapidly intensifying tropical cyclones. *Bull. Amer. Meteor. Soc.*, **101**, E1497–E1511, https://doi.org/10.1175/BAMS-D-19-0303.1.

Bister, M., and K. A. Emanuel, 1998: Dissipative heating and hurricane intensity. *Meteor. Atmos. Phys.*, **65**, 233–240, https://doi.org/10.1007/BF01030791.

Black, P. G., and Coauthors, 2007: Air–sea exchange in hurricanes: Synthesis of observations from the Coupled Boundary Layer Air–Sea Transfer experiment. *Bull. Amer. Meteor. Soc.*, **88**, 357–374, https://doi.org/10.1175/BAMS-88-3-357.

Bukunt, B. P., and G. M. Barnes, 2015: The subtropical jet stream delivers the coup de grâce to Hurricane Felicia (2009). *Wea. Forecasting*, **30**, 1039–1049, https://doi.org/10.1175/WAF-D-15-0004.1.

Carrasco, C. A., C. W. Landsea, and Y. Lin, 2014: The influence of tropical cyclone size on its intensification. *Wea. Forecasting*, **29**, 582–590, https://doi.org/10.1175/WAF-D-13-00092.1.

Chan, K. T., and J. C. Chan, 2012: Size and strength of tropical cyclones as inferred from QuikSCAT data. *Mon. Wea. Rev.*, **140**, 811–824, https://doi.org/10.1175/MWR-D-10-05062.1.

Chang, C.-C., and C.-C. Wu, 2017: On the processes leading to the rapid intensification of Typhoon Megi (2010). *J. Atmos. Sci.*, **74**, 1169–1200, https://doi.org/10.1175/JAS-D-16-0075.1.

Chang, Y.-T., I.-I. Lin, H.-C. Huang, Y.-C. Liao, and C.-C. Lien, 2020: The association of typhoon intensity increase with translation speed increase in the South China Sea. *Sustainability*, **12**, 939, https://doi.org/10.3390/su12030939.

Chavas, D. R., and K. A. Emanuel, 2010: A QuikSCAT climatology of tropical cyclone size. *Geophys. Res. Lett.*, **37**, L18816, https://doi.org/10.1029/2010GL044558.

Chen, D. Y.-C., K. K. W. Cheung, and C.-S. Lee, 2011: Some implications of core regime wind structures in western North Pacific tropical cyclones. *Wea. Forecasting*, **26**, 61–75, https://doi.org/10.1175/2010WAF2222420.1.

Chen, X., M. Xue, and J. Fang, 2018: Rapid intensification of Typhoon Mujigae (2015) under different sea surface temperatures: Structural changes leading to rapid intensification. *J. Atmos. Sci.*, **75**, 4313–4335, https://doi.org/10.1175/JAS-D-18-0017.1.

Cheng, C.-J., and C.-C. Wu, 2020: The role of WISHE in the rapid intensification of tropical cyclones. *J. Atmos. Sci.*, **77**, 3139–3160, https://doi.org/10.1175/JAS-D-20-0006.1.

Chih, C.-H., and C.-C. Wu, 2020: Exploratory analysis of upper ocean heat content and sea surface temperature underlying tropical cyclone rapid intensification in the western North Pacific. *J. Climate*, **33**, 1031–1050, https://doi.org/10.1175/JCLI-D-19-0305.1.

Cione, J. J., 2015: The relative roles of the ocean and atmosphere as revealed by buoy air–sea observations in hurricanes. *Mon. Wea. Rev.*, **143**, 904–913, https://doi.org/10.1175/MWR-D-13-00380.1.

——, and E. W. Uhlhorn, 2003: Sea surface temperature variability in hurricanes: Implications with respect to intensity change. *Mon. Wea. Rev.*, **131**, 1783–1796, https://doi.org/10.1175//2562.1.

D'Asaro, E. A., and Coauthors, 2014: Impact of typhoons on the ocean in the Pacific: ITOP. *Bull. Amer. Meteor. Soc.*, **95**, 1405–1418, https://doi.org/10.1175/BAMS-D-12-00104.1.

DeMaria, M., M. Mainelli, L. K. Shay, J. A. Knaff, and J. Kaplan, 2005: Further improvement to the Statistical Hurricane Intensity Prediction Scheme (SHIPS). *Wea. Forecasting*, **20**, 531–543, https://doi.org/10.1175/WAF862.1.

Dougherty, E. M., J. Molinari, R. F. Rogers, J. A. Zhang, and J. P. Kossin, 2018: Hurricane Bonnie (1998): Maintaining intensity during high vertical wind shear and an eyewall replacement cycle. *Mon. Wea. Rev.*, **146**, 3383–3399, https://doi.org/10.1175/MWR-D-18-0030.1.

Emanuel, K. A., 1989: The finite-amplitude nature of tropical cyclogenesis. *J. Atmos. Sci.*, **46**, 3431–3456, https://doi.org/10.1175/1520-0469(1989)046<3431:TFANOT>2.0.CO;2.

Fischer, M. S., R. F. Rogers, and P. D. Reasor, 2020: The rapid intensification and eyewall replacement cycles of Hurricane Irma (2017). *Mon. Wea. Rev.*, **148**, 981–1004, https://doi.org/10.1175/MWR-D-19-0185.1.

Frank, W. M., and E. A. Ritchie, 2001: Effects of vertical wind shear on the intensity and structure of numerically simulated hurricanes. *Mon. Wea. Rev.*, **129**, 2249–2269, https://doi.org/10.1175/1520-0493(2001)129<2249:EOVWSO>2.0.CO;2.

Goni, G., and Coauthors, 2009: Application of satellite-derived ocean measurements to tropical cyclone intensity forecasting. *Oceanography*, **22** (3), 190–197, https://doi.org/10.5670/oceanog.2009.78.

Hawkins, J. D., and M. Helveston, 2008: Tropical cyclone multiple eyewall characteristics. *28th Conf. on Hurricanes and Tropical Meteorology*, Orlando, FL, Amer. Meteor. Soc., P1.7, https://ams.confex.com/ams/26HURR/techprogram/paper_76084.htm.

Holliday, C. R., and A. H. Thompson, 1979: Climatological characteristics of rapidly intensifying typhoons. *Mon. Wea. Rev.*, **107**, 1022–1034, https://doi.org/10.1175/1520-0493(1979)107<1022:CCORIT>2.0.CO;2.

Hu, C.-C., and C.-C. Wu, 2020: Ensemble sensitivity analysis of tropical cyclone intensification rate during the development stage. *J. Atmos. Sci.*, **77**, 3387–3405, https://doi.org/10.1175/JAS-D-19-0196.1.

Huang, H.-C., J. Boucharel, I.-I. Lin, F.-F. Jin, C.-C. Lien, and I.-F. Pun, 2017: Air-sea fluxes for Hurricane Patricia (2015): Comparison with Supertyphoon Haiyan (2013) and under different ENSO conditions. *J. Geophys. Res. Oceans*, **122**, 6076–6089, https://doi.org/10.1002/2017JC012741.

Huang, P., I.-I. Lin, C. Chou, and R.-H. Huang, 2015: Change in ocean subsurface environment to suppress tropical cyclone intensification under global warming. *Nat. Commun.*, **6**, 7188, https://doi.org/10.1038/ncomms8188.

Ito, K., T. Kuroda, K. Saito, and A. Wada, 2015: Forecasting a large number of tropical cyclone intensities around Japan using a high-resolution atmosphere–ocean coupled model. *Wea. Forecasting*, **30**, 793–808, https://doi.org/10.1175/WAF-D-14-00034.1.

——, and Coauthors, 2018: Analysis and forecast using dropsonde data from the inner-core region of Tropical Cyclone Lan (2017) obtained during the first aircraft missions of T-PARCII. *SOLA*, **14**, 105–110, https://doi.org/10.2151/sola.2018-018.

Jaimes, B., L. K. Shay, and E. W. Uhlhorn, 2015: Enthalpy and momentum fluxes during Hurricane Earl relative to underlying ocean features. *Mon. Wea. Rev.*, **143**, 111–131, https://doi.org/10.1175/MWR-D-13-00277.1.

Kanada, S., S. Tsujino, H. Aiki, M. K. Yoshioka, Y. Miyazawa, K. Tsuboki, and I. Takayabu, 2017: Impacts of SST patterns on rapid intensification of Typhoon Megi (2010). *J. Geophys. Res. Atmos.*, **122**, 13 245–13 262, https://doi.org/10.1002/2017JD027252.

Kaplan, J., and M. DeMaria, 2003: Large-scale characteristics of rapidly intensifying tropical cyclones in the North Atlantic basin. *Wea. Forecasting*, **18**, 1093–1108, https://doi.org/10.1175/1520-0434(2003)018<1093:LCORIT>2.0.CO;2.

——, ——, and J. A. Knaff, 2010: A revised tropical cyclone rapid intensification index for the Atlantic and eastern North Pacific basins. *Wea. Forecasting*, **25**, 220–241, https://doi.org/10.1175/2009WAF2222280.1.

Knaff, J. A., C. R. Sampson, and M. DeMaria, 2005: An operational statistical typhoon intensity prediction scheme for the western North Pacific. *Wea. Forecasting*, **20**, 688–699, https://doi.org/10.1175/WAF863.1.

——, M. DeMaria, C. R. Sampson, J. E. Peak, J. Cummings, and W. H. Schubert, 2013: Upper oceanic energy response to tropical cyclone passage. *J. Climate*, **26**, 2631–2650, https://doi.org/10.1175/JCLI-D-12-00038.1.

——, C. J. Slocum, K. D. Musgrave, C. R. Sampson, and B. R. Strahl, 2016: Using routinely available information to estimate tropical cyclone wind structure. *Mon. Wea. Rev.*, **144**, 1233–1247, https://doi.org/10.1175/MWR-D-15-0267.1.

——, C. R. Sampson, and K. D. Musgrave, 2018: An operational rapid intensification prediction aid for the western North Pacific. *Wea. Forecasting*, **33**, 799–811, https://doi.org/10.1175/WAF-D-18-0012.1.

Ko, D. S., S.-Y. Chao, C.-C. Wu, and I-I Lin, 2014: Impacts of typhoon Megi (2010) on the South China Sea. *J. Geophys. Res. Oceans*, **119**, 4474–4489, https://doi.org/10.1002/2013JC009785.

Kossin, J. P., and M. Sitkowski, 2009: An objective model for identifying secondary eyewall formation in hurricanes. *Mon. Wea. Rev.*, **137**, 876–892, https://doi.org/10.1175/2008MWR2701.1.

——, and M. DeMaria, 2016: Reducing operational hurricane intensity forecast errors during eyewall replacement cycles. *Wea. Forecasting*, **31**, 601–608, https://doi.org/10.1175/WAF-D-15-0123.1.

——, J. A. Knaff, H. I. Berger, D. C. Herndon, T. A. Cram, C. S. Velden, R. J. Murnane, and J. D. Hawkins, 2007: Estimating hurricane wind structure in the absence of aircraft reconnaissance. *Wea. Forecasting*, **22**, 89–101, https://doi.org/10.1175/WAF985.1.

Kuo, H.-C., C.-P. Chang, Y.-T. Yang, and H.-J. Jiang, 2009: Western North Pacific typhoons with concentric eyewalls. *Mon. Wea. Rev.*, **137**, 3758–3770, https://doi.org/10.1175/2009MWR2850.1.

——, S. Tsujino, C.-C. Wang, C.-C. Huang, and K. Tsuboki, 2019: Diagnosis of the dynamic efficiency of latent heat release and the rapid intensification of Supertyphoon Haiyan (2013). *Mon. Wea. Rev.*, **147**, 1127–1147, https://doi.org/10.1175/MWR-D-18-0149.1.

Lagmay, A. M. F., and Coauthors, 2015: Devastating storm surges of Typhoon Haiyan. *Int. J. Disaster Risk Reduct.*, **11**, 1–12, https://doi.org/10.1016/j.ijdrr.2014.10.006.

Lander, M., C. Guard, and S. J. Camargo, 2014: Tropical cyclones, Super-Typhoon Haiyan, [in "State of the Climate in 2013"]. *Bull. Amer. Meteor. Soc.*, **95**, S112–S114, https://doi.org/10.1175/2014BAMSStateoftheClimate.1.

Lin, I.-I., C.-C. Wu, K. Emanuel, I.-H. Lee, C.-R. Wu, and I.-F. Pun, 2005: The interaction of Supertyphoon Maemi (2003) with a warm ocean eddy. *Mon. Wea. Rev.*, **133**, 2635–2649, https://doi.org/10.1175/MWR3005.1.

——, ——, I.-F. Pun, and D. S. Ko, 2008: Upper-ocean thermal structure and the western North Pacific category 5 typhoons. Part I: Ocean features and the category 5 typhoons' intensification. *Mon. Wea. Rev.*, **136**, 3288–3306, https://doi.org/10.1175/2008MWR2277.1.

——, C.-H. Chen, I.-F. Pun, W. T. Liu, and C.-C. Wu, 2009a: Warm ocean anomaly, air sea fluxes, and the rapid intensification of Tropical Cyclone Nargis (2008). *Geophys. Res. Lett.*, **36**, L03817, https://doi.org/10.1029/2008GL035815.

——, I.-F. Pun, and C.-C. Wu, 2009b: Upper ocean thermal structure and the western North Pacific category-5 typhoons Part II: Dependence on translation speed. *Mon. Wea. Rev.*, **137**, 3744–3757, https://doi.org/10.1175/2009MWR2713.1.

——, G. J. Goni, J. Knaff, C. Forbes, and M. M. Ali, 2013a: Ocean heat content for tropical cyclone intensity forecasting and its impact on storm surge. *Nat. Hazards*, **66**, 1481–1500, https://doi.org/10.1007/s11069-012-0214-5.

——, and Coauthors, 2013b: An ocean coupling potential intensity index for tropical cyclones. *Geophys. Res. Lett.*, **40**, 1878–1882, https://doi.org/10.1002/grl.50091.

——, I.-F. Pun, and C.-C. Lien, 2014: "Category-6" Supertyphoon Haiyan in global warming hiatus: Contribution from subsurface ocean warming. *Geophys. Res. Lett.*, **41**, 8547–8553, https://doi.org/10.1002/2014GL061281.

Marks, F. D., and Coauthors, 1998: Landfalling tropical cyclones: Forecast problems and associated research opportunities. *Bull. Amer. Meteor. Soc.*, **79**, 305–323, https://doi.org/10.1175/1520-0477(1998)079<0285:QPFROT>2.0.CO;2.

Martinez, J., M. M. Bell, J. L. Vigh, and R. F. Rogers, 2017: Examining tropical cyclone structure and intensification with the FLIGHT+ dataset from 1999 to 2012. *Mon. Wea. Rev.*, **145**, 4401–4421, https://doi.org/10.1175/MWR-D-17-0011.1.

Mei, W., C.-C. Lien, I-I Lin, and S.-P. Xie, 2015: Tropical cyclone-induced ocean response: A comparative study of the South China Sea and tropical Northwest Pacific. *J. Climate*, **28**, 5952–5968.

Miyamoto, Y., and T. Takemi, 2015: A triggering mechanism for rapid intensification of tropical cyclones. *J. Atmos. Sci.*, **72**, 2666–2681, https://doi.org/10.1175/JAS-D-14-0193.1.

Molinari, J., J. A. Zhang, R. F. Rogers, and D. Vollaro, 2019: Repeated eyewall replacement cycles in Hurricane Frances (2004). *Mon. Wea. Rev.*, **147**, 2009–2022, https://doi.org/10.1175/MWR-D-18-0345.1.

Mori, N., M. Kato, S. Kim, H. Mase, Y. Shibutani, T. Takemi, K. Tsuboki, and T. Yasuda, 2014: Local amplification of storm surge by Super Typhoon Haiyan in Leyte Gulf. *Geophys. Res. Lett.*, **41**, 5106–5113, https://doi.org/10.1002/2014GL060689.

Pendergrass, A. G., and H. E. Willoughby, 2009: Diabatically induced secondary flows in tropical cyclones. Part I: Quasi-steady forcing. *Mon. Wea. Rev.*, **137**, 805–821, https://doi.org/10.1175/2008MWR2657.1.

Peng, C.-H., and C.-C. Wu, 2020: The impact of outer-core surface heat fluxes on the convective activities and rapid intensification of tropical cyclones. *J. Atmos. Sci.*, **77**, 3907–3927, https://doi.org/10.1175/JAS-D-19-0348.1.

Powell, M. D., P. J. Vickery, and T. A. Reinhold, 2003: Reduced drag coefficient for high wind speeds in tropical cyclones. *Nature*, **422**, 279–283, https://doi.org/10.1038/nature01481.

Price, J. F., 1981: Upper ocean response to a hurricane. *J. Phys. Oceanogr.*, **11**, 153–175, https://doi.org/10.1175/1520-0485(1981)011<0153:UORTAH>2.0.CO;2.

——, R. A. Weller, and R. Pinkel, 1986: Diurnal cycling: Observations and models of the upper ocean response to diurnal heating, cooling, and wind mixing. *J. Geophys. Res.*, **91**, 8411–8427, https://doi.org/10.1029/JC091iC07p08411.

——, T. B. Sanford, and G. Z. Forristall, 1994: Forced stage response to a moving hurricane. *J. Phys. Oceanogr.*, **24**, 233–260, https://doi.org/10.1175/1520-0485(1994)024<0233:FSRTAM>2.0.CO;2.

Pun, I.-F., I-I Lin, C.-R. Wu, D.-S. Ko, and W.-T. Liu, 2007: Validation and application of altimetry-derived upper ocean thermal structure in the Western North Pacific Ocean for typhoon intensity forecast. *IEEE Trans. Geosci. Remote Sens.*, **45**, 1616–1630, https://doi.org/10.1109/TGRS.2007.895950.

——, Y.-T. Chang, I-I Lin, T.-Y. Tang, and R.-C. Lien, 2011: Typhoon-ocean interaction in the Western North Pacific: Part 2. *Oceanogr.*, **24**, 32–41, https://doi.org/10.5670/oceanog.2011.92.

——, I-I Lin, and M.-H. Lo, 2013: Recent increase in high tropical cyclone heat potential area in the Western North Pacific Ocean. *Geophy. Res. Lett.*, **40**, 4680-4684, https://doi.org/10.1002/grl.50548.

——, ——, and D. S. Ko, 2014: New generation of satellite-derived ocean thermal structure for the western North Pacific typhoon intensity forecasting. *Prog. Oceanogr.*, **121**, 109–124, https://doi.org/10.1016/j.pocean.2013.10.004.

——, ——, C.-C. Lien, and C.-C. Wu, 2018: Influence of the size of Supertyphoon Megi (2010) on SST cooling. *Mon. Wea. Rev.*, **146**, 661–677, https://doi.org/10.1175/MWR-D-17-0044.1.

——, and Coauthors, 2019: Rapid intensification of Typhoon Hato (2017) over shallow water. *Sustainability*, **11**, 3709, https://doi.org/10.3390/su11133709.

Rogers, R., 2010: Convective-scale structure and evolution during a high-resolution simulation of tropical cyclone rapid intensification. *J. Atmos. Sci.*, **67**, 44–70, https://doi.org/10.1175/2009JAS3122.1.

——, and Coauthors, 2006: The Intensity Forecasting Experiment: A NOAA multiyear field program for improving tropical cyclone intensity forecast. *Bull. Amer. Meteor. Soc.*, **87**, 1523–1538, https://doi.org/10.1175/BAMS-87-11-1523.

——, P. Reasor, and S. Lorsolo, 2013: Airborne doppler observations of the inner-core structural differences between intensifying and steady-state tropical cyclones. *Mon. Wea. Rev.*, **141**, 2970–2991, https://doi.org/10.1175/MWR-D-12-00357.1.

——, ——, and J. A. Zhang, 2015: Multiscale structure and evolution of Earl (2010) during rapid intensification. *Mon. Wea. Rev.*, **143**, 536–562, https://doi.org/10.1175/MWR-D-14-00175.1.

——, J. A. Zhang, J. Zawislak, H. Jiang, G. R. Alvey III, E. J. Zipser, and S. N. Stevenson, 2016: Observations of the structure and evolution of Hurricane Edouard (2014) during intensity change. Part II: Kinematic structure and the distribution of deep convection. *Mon. Wea. Rev.*, **144**, 3355–3376, https://doi.org/10.1175/MWR-D-16-0017.1.

——, and Coauthors, 2017: Rewriting the tropical record books: The extraordinary intensification of Hurricane Patricia. *Bull. Amer. Meteor. Soc.*, **98**, 2091–2112, https://doi.org/10.1175/BAMS-D-16-0039.1.

Rozoff, C. M., D. S. Nolan, J. P. Kossin, F. Zhang, and J. Fang, 2012: The roles of an expanding wind field and inertial stability in tropical cyclone secondary eyewall formation. *J. Atmos. Sci.*, **69**, 2621–2643, https://doi.org/10.1175/JAS-D-11-0326.1.

Sampson, C. R., E. M. Fukada, J. A. Knaff, B. R. Strahl, M. J. Brennan, and T. Marchok, 2017: Tropical cyclone gale wind radii estimates for the western North

Pacific. *Wea. Forecasting*, **32**, 1029–1040, https://doi.org/10.1175/WAF-D-16-0196.1.

Shay, L. K., and J. K. Brewster, 2010: Oceanic heat content variability in the eastern Pacific Ocean for hurricane intensity forecasting. *Mon. Wea. Rev.*, **138**, 2110–2131, https://doi.org/10.1175/2010MWR3189.1.

——, G. J. Goni, and P. G. Black, 2000: Role of a warm ocean feature on Hurricane Opal. *Mon. Wea. Rev.*, **128**, 1366–1383, https://doi.org/10.1175/1520-0493(2000)128<1366:EOAWOF>2.0.CO;2.

Shen, L.-Z., C.-C. Wu, and F. Judt, 2021: The role of surface heat fluxes on the size of Typhoon Megi (2016). *J. Atmos. Sci.*, **78**, 1075–1093, https://doi.org/10.1175/JAS-D-20-0141.1.

Sitkowski, M., J. P. Kossin, and C. M. Rozoff, 2011: Intensity and structure changes during hurricane eyewall replacement cycles. *Mon. Wea. Rev.*, **139**, 3829–3847, https://doi.org/10.1175/MWR-D-11-00034.1.

Smith, R. K., and M. T. Montgomery, 2016: The efficiency of diabatic heating and tropical cyclone intensification. *Quart. J. Roy. Meteor. Soc.*, **142**, 2081–2086, https://doi.org/10.1002/qj.2804.

Tsuboki, K., M. K. Yoshioka, T. Shinoda, M. Kato, S. Kanada, and A. Kitoh, 2015: Future increase of supertyphoon intensity associated with climate change. *Geophys. Res. Lett.*, **42**, 646–652, https://doi.org/10.1002/2014GL061793.

Tsujino, S., and H.-C. Kuo, 2020: Potential vorticity mixing and rapid intensification in numerically simulated Supertyphoon Haiyan (2013). *J. Atmos. Sci.*, **77**, 2067–2090, https://doi.org/10.1175/JAS-D-19-0219.1.

Vigh, J. L., and W. H. Schubert, 2009: Rapid development of the tropical cyclone warm core. *J. Atmos. Sci.*, **66**, 3335–3350, https://doi.org/10.1175/2009JAS3092.1.

Wada, A., S. Kanada, and H. Yamada, 2018: Effect of air-sea environmental conditions and interfacial processes on extremely intense Typhoon Haiyan (2013). *J. Geophys. Res. Atmos.*, **123**, 10379–10405, https://doi.org/10.1029/2017JD028139.

Walker, N. D., R. R. Leben, C. T. Pilley, M. Shannon, D. C. Herndon, I.-F. Pun, I-I Lin, and C. L. Gentemann, 2014: Slow translation speed causes rapid collapse of northeast Pacific Hurricane Kenneth over cold core eddy. *Geophy. Res. Lett.*, **41**, 7595–7601, https://doi.org/10.1002/2014GL061584.

Wang, Y., 2009: How do outer spiral rainbands affect tropical cyclone structure and intensity? *J. Atmos. Sci.*, **66**, 1250–1273, https://doi.org/10.1175/2008JAS2737.1.

Wimmers, A. J., and C. S. Velden, 2016: Advancements in objective multisatellite tropical cyclone center fixing. *J. Appl. Meteor. Climatol.*, **55**, 197–212, https://doi.org/10.1175/JAMC-D-15-0098.1.

——, S. Griffin, J. Gerth, S. Bachmeier, and S. Lindstrom, 2018: Observations of gravity waves with high-pass filtering in the new generation of geostationary imagers and their relation to aircraft turbulence. *Wea. Forecasting*, **33**, 139–144, https://doi.org/10.1175/WAF-D-17-0080.1.

Wu, C.-C., and Coauthors, 2005: Dropwindsonde observations for typhoon surveillance near the Taiwan region (DOTSTAR): an overview. *Bull. Amer. Meteor. Soc.*, **86**, 787–790, https://doi.org/ 10.1175/BAMS-86-6-787.

Wu, C.-C., C.-Y. Lee, and I.-I. Lin, 2007: The effect of the ocean eddy on tropical cyclone intensity. *J. Atmos. Sci.*, **64**, 3562–3578, https://doi.org/10.1175/JAS4051.1.

——, W.-T. Tu, I.-F. Pun, I.-I. Lin, and M.-S. Peng, 2016: Tropical cyclone-ocean interaction in Typhoon Megi (2010)—A synergy study based on ITOP observations and atmosphere-ocean coupled model simulations. *J. Geophys. Res. Atmos.*, **121**, 153–167, https://doi.org/10.1002/2015JD024198.

Xu, J., and Y. Wang, 2018: Dependence of tropical cyclone intensification rate on sea surface temperature, storm intensity, and size in the western North Pacific. *Wea. Forecasting*, **33**, 523–537, https://doi.org/10.1175/WAF-D-17-0095.1.

Zhang, J. A., P. G. Black, J. R. French, and W. M. Drennan, 2008: First direct measurements of enthalpy flux in the hurricane boundary layer: The CBLAST results. *Geophys. Res. Lett.*, **35**, L14813, https://doi.org/10.1029/2008GL034374.

——, R. F. Rogers, P. D. Reasor, E. W. Uhlhorn, and F. D. Marks, 2013: Asymmetric hurricane boundary layer structure from dropsonde composites in relation to the environmental vertical wind shear. *Mon. Wea. Rev.*, **141**, 3968–3984, https://doi.org/10.1175/MWR-D-12-00335.1.

——, J. J. Cione, E. A. Kalina, E. W. Uhlhorn, T. Hock, and J. A. Smith, 2017: Observations of infrared sea surface temperature and air–sea interaction in Hurricane Edouard (2014) using GPS dropsondes. *J. Atmos. Oceanic Technol.*, **34**, 1333–1349, https://doi.org/10.1175/JTECH-D-16-0211.1.

——, J. P. Dunion, and D. S. Nolan, 2020: In situ observations of the diurnal variation in the boundary layer of mature hurricanes. *Geophys. Res. Lett.*, **47**, 2019GL086206, https://doi.org/10.1029/2019GL086206.

Zheng, Z.-W., I-I Lin, B. Wang, H.-C. Huang, and C.-H. Chen, 2015: A Long Neglected Damper in the El Niño—Typhoon Relationship: a 'Gaia-Like' Process. *Sci. Rep.*, **5**, 11103, https://doi.org/10.1038/srep11103.